UNIVERSIDADE DE SÃO PAULO ESCOLA POLITÉCNICA
DEPARTAMENTO DE ENGENHARIA MECÂNICA

ANALYSIS OF THE INFLUENCE OF COMPRESSIBILITY ON THE AERODYNAMIC CENTER IN THE TRANSONIC REGIME

Jonis Qasem

São Paulo

2017

UNIVERSIDADE DE SÃO PAULO ESCOLA POLITÉCNICA
DEPARTAMENTO DE ENGENHARIA MECÂNICA

Analysis of the influence of compressibility on the aerodynamic center in the transonic regime

Trabalho de formatura apresentado à Escola Politécnica da Universidade de São Paulo para a obtenção do título de Graduação em Engenharia.

Jonis Qasem

Orientador: Prof. Ernani Vitillo Volpe

Área de concentração:
Engenharia Mecânica

São Paulo

2017

Catalogação-na-publicação

Qasem, Jonis
Analysis of the influence of compressibility on the aerodynamic center in the transonic regime / J. Qasem -- São Paulo, 2017.
75 p.

Trabalho de Formatura - Escola Politécnica da Universidade de São Paulo. Departamento de Engenharia Mecânica.

Volte e preencha o campo Assuntol.Universidade de São Paulo. Escola Politécnica. Departamento de Engenharia Mecânica II.t.

ABSTRACT

Air traffic is growing almost exponentially and new civil aircrafts have brought revolutionary advancements, yet subsonic jets fly no faster than in the 1970s. This is due to the complexity of compressibility effects within the transonic regime. Aerodynamicists have put a great amount of research effort into this topic and although the behavior of transonic flow is nowadays understood, uncertainties remain about quantitative predictions. These uncertainties arise mainly due to the non-linearity of the governing flow equations. This work aims to study the influence of compressibility on the aerodynamic center for 2-D airfoils at transonic speeds (Mach 0.60-0.95). Available Computational Fluid Dynamics codes based on the Euler equations and the adjoint method are used to study these effects for the airfoils NACA 0012 and RAE 2822. A study of the governing equations and a bibliographical review of available research is conducted, in order to compare and validate the obtained results. These results will be used as input for the adjoint method, to study the sensitivities of the aerodynamic center with respect to stagnation pressure and stagnation temperature.

Keywords: Aerodynamics, Transonic Flow, Aerodynamic Center, Adjoint Method

LIST OF FIGURES

LIST OF TABLES

LIST OFABREVIATIONS AND ACRONYMS

CFD Computational Fluid Dynamics

RHS Right Hand Side

AC Aerodynamic Center

CG Center of Gravity

Cp Pressure Coefficient

$\mathbf{x_{ac}}$ x-coordinate of the aerodynamic center

$\mathbf{z_{ac}}$ z-coordinate of the aerodynamic center

$\mathbf{M_{ac}}$ Moment about the aerodynamic center

$\mathbf{T_0}$ Stagnation Temperature

$\mathbf{p_0}$ Stagnation Pressure

TABLE OF CONTENT

1. INTRODUCTION

Airflows are called transonic flows when local velocities are reached, that are close to the speed of sound (sonic). In the same flow field, a mixed sub- and supersonic local flow occurs. The ratio of the flow speed v to the speed of sound a is called the Mach number:

$$Ma = \frac{v}{a} \tag{1}$$

with $a = \sqrt{\gamma RT}$.

T being the absolute Temperature, R the gas constant and γ the ratio of specific heats.

Transonic flows therefore are flows where the Mach number is close to Ma = 1. This means that the static pressure and the dynamic pressure $\frac{\rho v^2}{2}$ have the same magnitude. In subsonic flows for slender bodies until a flow velocity of approximately Ma = 0.6 no significant changes in the behaviour of lift and drag for incompressible fluids occur. However, an increase to Mach numbers above Ma = 0.6 results in local supersonic velocities and shock waves. Hence the characteristics of the flow field change significantly. The freestream Mach number where local sonic conditions are first obtained somewhere on the airfoil surface is named the critical Mach number. It is a function of various parameters like shape, thickness, sweep and the lift coefficient of the wing. In Figure 1.1 the zero-drag coefficient is shown depending on the Mach number. The blue part represents the drag due to skin friction, the red part represents the form and interference drag, whereas the green part of the figure shows the wave drag. Once the critical Mach number Ma = Ma_{∞}^{*}, in this case Ma = 0.8, is reached, the wave drag starts increasing with the mere appearance of a locally supersonic flow region within the domain. With increasing Mach numbers shock waves appear in the flow field and get stronger as the velocity increases which leads to an almost exponential growth in wave drag. Therefore, the rapid increase in drag in the transonic regime is due to the emergence of wave drag and because the pressure rise through a shock wave thickens the boundary

layer, leading to an increase in viscous drag. For slender bodies, transonic flow occurs in the region of $0.8 \leq Ma \geq 1.2$.

The aerodynamic centre also begins to move along the chord after a critical Mach number is reached. As the aerodynamic centre is very important for the stability of the aircraft it is of great interest to know how this change of position occurs in the transonic regime. For an aircraft not designed to fly at the Critical Mach number, shock waves in the flow over the wing and tailplane can be sufficient to stall the wing, make control surfaces ineffective and lead to loss of control.(BÖSWIRTH, BSCHORER, 2014; COLE, COOK, 1986; SCHOLZ, CIORNEI, 2005)

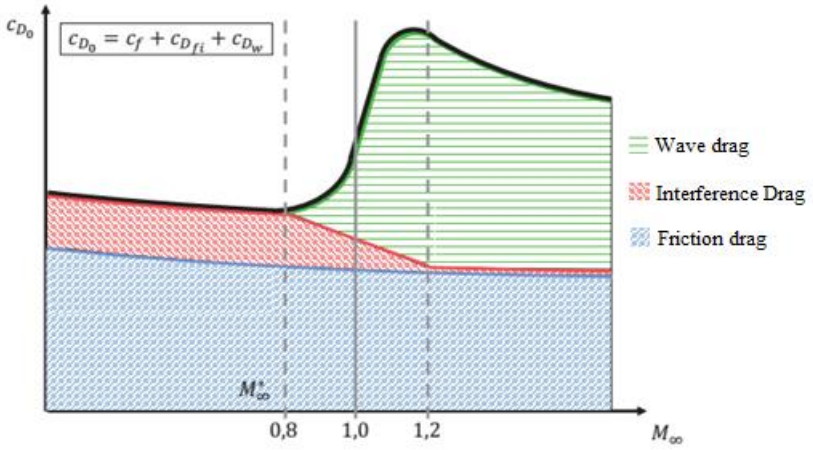

Figure 1.1 Drag coefficient over Mach number extracted from (HORNUNG, 2015)

When the first operational jet-propelled airplanes reached such velocities in 1944, the incompressible theory became inapplicable. To be able to use the large amount of data that already existed for low-speed aerodynamics, aerodynamicists searched for methods that would allow to take the effects of compressibility into account. These methods are called compressibility corrections. The Prandtl-Glauert-Correlation given by eq.(2) is such a compressibility correction based on the linearized perturbation velocity potential equation. It is limited to thin airfoils and small angles of attack, as well as it loses its applicability in the proximity of Ma = 1 where the flow characteristics lose their linearity.

$$\frac{dc_l}{d\alpha} = \frac{1}{\sqrt{1-M_\infty^2}}\frac{dc_l}{d\alpha}|_{ik} = \frac{2\pi}{\sqrt{1-M_\infty^2}} \tag{2}$$

Figure 1.2 shows an airfoil at increasing freestream velocities M_∞. The point A represents the location of the minimum pressure on the surface of the airfoil and therefore as well the maximum Mach number M_A. By increasing M_∞, M_A also increases. For the airfoil in Figure 1.2 the corresponding local Mach number M_A to a freestream velocity of M_∞= 0.3 and M_∞ = 0.5, is respectively M_A = 0.435 and M_A = 0.772. It can be seen that $M_A \geqslant M_\infty$, hence M_A= 1 is reached at subsonic freestream velocities respectively M_∞ = 0.61 in Figure 1.2.. Equally to the critical Mach number, the critical pressure coefficient is the value of the pressure coefficient when M_A= 1 is reached. The formula is:

$$c_{p,crit} = \frac{2}{\gamma M_\infty^2}\left\{\left(\frac{1+((\gamma-1)/2)M_\infty^2}{1+(\frac{\gamma-1}{2})}\right)^{\frac{\gamma}{\gamma-1}} - 1\right\}. \tag{3}$$

It establishes a relation between the freestream velocity and the pressure coefficient on the profile surface at local Ma = 1. (Anderson, 2001)

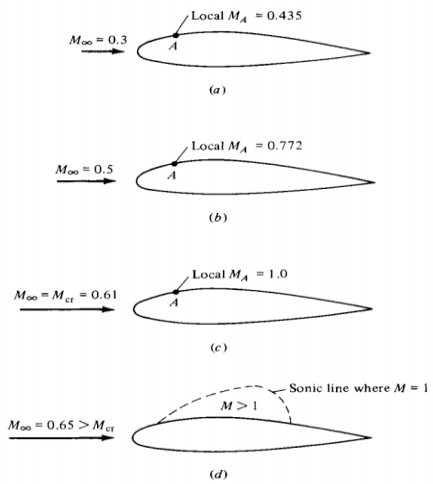

Figure 1.2 Definition of critical Mach number. Point A represents the location of minimum pressure on the top surface of the airfoil. Extracted from (Anderson, 2001)

2. FLOW EQUATIONS

2.1. THE CONINUITY EQUATION

Mass can neither be created nor destroyed. This means that the mass of a fluid element remains constant, even though its shape, volume and density may change. The total mass within the control volume R, which is fixed in the field is:

$$\iiint_R \rho \, dR \tag{4}$$

On the control surface, the mass flow per unit time through any incremental area dS is $\rho V * ndS$. The net efflux of mass through the surface S must be equal to the decrease of mass within R. Therefore, the conservation of mass in terms of field properties is

$$\iint_S \rho \vec{u} \cdot \vec{n} \, dS = -\iiint_R \frac{\delta \rho}{\delta t} \, dR \tag{5}$$

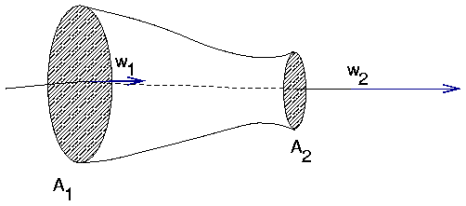

Figure 2.1 Conservation of Mass extracted from (JUNGLAS)

Applying the above principle to a steady flow in a tube as shown in Figure 2.1, with no flux through the wall and by assuming that ρ_1 and u_1 as well as ρ_2 and u_2 are average values across the areas A_1 and A_2 the conservation of mass principle becomes

$$\rho_2 u_2 A_2 - \rho_1 u_1 A_1 = 0 \tag{6}$$

If the divergence theorem by Gauss is applied to the surface integral in eq.(5) it can be transformed into a volume integral:

$$\iint_S \rho\vec{u} \cdot \vec{n}\, dS = \iiint_R div\rho\vec{u}\, dR \tag{7}$$

Therefore, eq. (5) can be written in the form

$$\iiint_R \left(div\rho\vec{u} + \frac{\delta\rho}{\delta t} \right) dR = 0 \tag{8}$$

As eq.(8) holds for all control volumes regardless of size the integrand must be zero. Then the equation of continuity, which is a statement of the conservation of mass principle is obtained as a differential equation:

$$div\rho\vec{u} + \frac{\delta\rho}{\delta t} = 0 \tag{9}$$

(KUETHE, CHOW, 1998)

2.2. THE MOMENTUM EQUATION

The application of Newtons Law on fluid volume $\tilde{V}$ means: The temporal change in momentum of a fluid volume $\tilde{V}$ is equal to the resultant of the forces acting on it.

The moment

um vector is given by

$$\vec{P} = \int_{\tilde{V}} \rho\vec{u}\, dV \tag{10}$$

and the temporal change in momentum is

$$\frac{d\vec{P}}{dt} = \frac{d}{dt}\int_{\tilde{V}} \rho\vec{u}dV = \sum_m \vec{F}_m \ . \tag{11}$$

Possible forces that may occur are:

- volume forces acting on every fluid element represented by

$$\vec{F}_V = \int_{\tilde{V}} \rho\vec{f}\, dV \tag{12}$$

- forces acting on the body in isolated points

$$\vec{F}_K \tag{13}$$

- surface forces distributed over the surface $\tilde{S}$ of $\tilde{V}$

$$\vec{F}_S = \int_{\tilde{S}} \sigma^T \cdot \vec{n}\, dS \ . \tag{14}$$

Hereby σ is a second order tensor in the form of

$$\sigma = -pI + \tau = \begin{bmatrix} -p+\tau_{11} & \tau_{12} & \tau_{13} \\ \tau_{21} & -p+\tau_{22} & \tau_{23} \\ \tau_{31} & \tau_{32} & -p+\tau_{33} \end{bmatrix} \tag{15}$$

where p represents the pressure, I the identity vector and

$$\tau = \begin{bmatrix} \tau_{11} & \tau_{12} & \tau_{13} \\ \tau_{21} & \tau_{22} & \tau_{23} \\ \tau_{31} & \tau_{32} & \tau_{33} \end{bmatrix}$$

the stress tensor. The diagonal components of τ are the normal stresses, while the other components are the shear stresses.

The second stage tensor σ is symmetric and therefore $\sigma = \sigma^T$ or $\tau_{ij} = \tau_{ji}$.

This characteristic is going to be used from now on. The application of the Reynolds-Transport-Theorem on every component P_i of

$$\vec{P} = \begin{bmatrix} P_1 \\ P_2 \\ P_3 \end{bmatrix}$$

with

$$P_i = \int_{\tilde{V}} \rho u_i dV$$

results in:

$$\frac{dP_i}{dt} = \int_V \frac{\partial \rho u_i}{\partial t} dV + \int_S \tau u_i (\vec{u} \cdot \vec{n}) dS \,. \tag{16}$$

All components i = 1,2,3 brought together in a vector gives us the momentum equation in the integral notation:

$$\begin{aligned} \frac{d\vec{P}}{dt} &= \int_V \frac{\partial \rho \vec{u}}{\partial t} dV + \int_S \rho \vec{u} (\vec{u} \cdot \vec{n}) dS = \sum_m \vec{F}_m \\ &= \int_S \sigma \cdot \vec{n} dS + \int_V \rho \vec{f} \, dV + \vec{F}_K \\ &= -\int_S \rho \cdot \vec{n} dS + \int_S \tau \cdot \vec{n} dS + \int_V \rho \vec{f} \, dV + \vec{F}_K \end{aligned} \tag{17}$$

The application of the Reynolds-Transport-Theorem to all components P_i of $\vec{P}$ results in

$$\int_V \left(\frac{\partial \rho \vec{u}}{\partial t} + \nabla \cdot (\rho \vec{u} \vec{u}) \right) dV = -\int_S \rho \cdot \vec{n} dS + \int_S \tau \cdot \vec{n} dS + \int_V \rho \vec{f} \, dV + \vec{F}_K \tag{18}$$

.

If now the Gauss´s theorem is applied on every i-component we get

$$\int_S \sigma \cdot \vec{n} dS = \int_V \nabla \cdot \sigma \, dV \; .$$

And with $\sigma = -pI + \tau$ we can transform eq.(18) into

$$\int_V \left(\frac{\partial \rho \vec{u}}{\partial t} + \nabla \cdot \left(\rho \vec{u} \vec{u} \right) \right) dV = \int_V \left(-\nabla p + \nabla \cdot \tau + \rho \vec{f} \right) dV + \vec{F}_K \tag{19}$$

If the forces acting on the body are $\vec{F}_K$ = 0 and an arbitrary volume V then

$$\frac{\partial \rho \vec{u}}{\partial t} + \nabla \cdot \left(\rho \vec{u} \vec{u} \right) = -\nabla p + \nabla \cdot \tau + \rho \vec{f} \tag{20}$$

must hold true.

In tensor notation eq.(18) becomes

$$\int_V \frac{\partial \rho u_i}{\partial t} dV + \int_S \rho u_i u_j n_j dS = -\int_S p n_i dS + \int_S \tau_{ij} n_j dS + \int_V \rho f_i \, dV + F_{K_i} \tag{21}$$

and eq.(20) is the momentum equation as a differential equation

$$\frac{\partial \rho u_i}{\partial t} + \frac{\partial \rho u_i u_j}{\partial x_j} = -\frac{\partial p}{\partial x_i} + \frac{\partial \tau_{ij}}{\partial x_j} + \rho f_i \; . \tag{22}$$

Using the continuum equation eq.(13), eq.(20) or eq.(22) can be written as

$$\frac{\partial \vec{u}}{\partial t} + \left(\vec{u} \cdot \nabla \right) \vec{u} = -\frac{1}{\rho} \nabla p + \frac{1}{\rho} \nabla \cdot \tau + \vec{f} \tag{23}$$

or

$$\frac{\partial u_i}{\partial t} + u_j \frac{\partial u_i}{\partial x_j} = -\frac{1}{\rho} \frac{\partial p}{\partial x_i} + \frac{1}{\rho} \frac{\partial \tau_{ij}}{\partial x_j} + f_i \tag{24}$$

2.3. THE ENERGY EQUATION

For incompressible flows ρ is constant and the primary flow variables are p and V. To study incompressible flow, the continuity and momentum equation are sufficient. But for compressible flows ρ is an extra variable that has to be considered and therefore another fundamental equation is needed.

The first law of thermodynamics, the law of conservation of energy expresses the balance of energy exchanges between a system and its surroundings. Hence, the rate of increase of energy E of a fluid element is equal to the rate W_1, where work is done on the element by body forces, plus W_2, where work is done on the elements surface by surface forces, plus W_3, which accounts for the heat transfer. This can be expressed as

$$\frac{DE}{Dt} = W_1 + W_2 + W_3 \tag{25}$$

The energy of the fluid per unit mass is

$$e + \frac{u^2}{2} \tag{26}$$

where $e = (r, t)$ represents the internal energy and $\frac{u^2}{2}$ the kinetic energy.

Hence, the energy of the fluid is given by

$$E = \rho \delta_\tau \left(e + \frac{u^2}{2} \right) \tag{27}$$

The work rate conducted through body forces is expressed by

$$W_1 = \rho \delta_\tau \, \vec{f} \cdot \vec{u} \tag{28}$$

We are considering an inviscid fluid, and therefore pressure forces are the only surface forces. Hence, the work rate conducted by surface forces is

$$W_2 = -\oiint_{\partial S} p\vec{n}\, dS \cdot \vec{u} = -\oiint_{\partial S} p\vec{u} \cdot \vec{n}\, dS \tag{29}$$

Eq.(29) applied to an infinitesimally small volume element becomes

$$W_2 = -\delta_\tau \, div\, \rho\vec{u} = -\delta_\tau (grad\ p \cdot \vec{u} + p\, div\vec{u}) \tag{30}$$

Hence, the rate of work conducted by the surface forces is equal to $-div\, \rho u$. This work can be subdivided into two parts where $-grad\ p \cdot u$ represents the rate at which work rate due to the resultant of the surfaces forces and $-p\, divu$ the work rate due to an increase in its volume. (KARAMCHETI, 1980)

Bringing eq. (25)(27)(28) and (30) together we are presented with

$$\frac{D}{Dt}\left[\rho\delta_\tau\left(e+\frac{u^2}{2}\right)\right] = \rho\delta_\tau\, \vec{f}\cdot\vec{u} - \delta_\tau\, grad\ p\cdot\vec{u} - \delta_\tau\, p\, div\vec{u} \tag{31}$$

and as the derivative of $\rho\delta\tau$ is zero,

$$\rho\,\delta_\tau \frac{D}{Dt}\left(e+\frac{u^2}{2}\right) = \rho\delta_\tau\, \vec{f}\cdot\vec{u} - \delta_\tau\, grad\ p\cdot\vec{u} - \delta_\tau\, p\, div\vec{u} \tag{32}$$

The equation of conservation of energy or, simply the equation of energy is obtained by expressing eq.(32) per unit volume

$$\rho\frac{D}{Dt}\left(e+\frac{u^2}{2}\right) = \rho\vec{f}\cdot\vec{u} - grad\ p\cdot\vec{u} - p\, div\vec{u} \tag{33}$$

2.4. THE NAVIER-STOKES EQUATIONS

Putting the previous results together we are presented with the Navier-Stokes equations:

$$\frac{D\rho}{Dt} = -\rho \nabla \cdot \vec{u} \tag{34}$$

$$\rho \frac{D\vec{u}}{Dt} = -\nabla p + \nabla \cdot \tau + \rho \vec{f} \tag{35}$$

$$\rho \frac{De}{Dt} = -\nabla \cdot \vec{f} - p\nabla \cdot \vec{u} + \tau : \nabla \cdot \vec{u} + pq''' \tag{36}$$

Equation (34) represents local mass conservation. Change in density of a Lagrangian fluid element occurs due to a change in specific volume.

Equation (35) represents local momentum conservation. Gravity, pressure gradients and viscous forces produce accelerations.

Equation (36) represents the local energy conservation, where the second law of thermodynamics is implicit. For Newtonian-Stokesian fluids changes in internal energy can be produced by work, conduction, viscous dissipation or viscous heating.

The Navier-Stokes equations are named after Claude-Louis Navier and George Gabriel Stokes and govern the motion of fluids. They are of great importance in computational fluid dynamics. Due to their complexity, only a limited number of analytical solutions exist. Hence, depending on the application simplification are adopted to solve the equations.(LORENZ, 1994)

2.5. EULER EQUATIONS

Around the 1750s Leonhard Euler presented a set of equations that solves the Navier-Stokes equations when the effects of viscosity and heat transfer are neglected. With zero viscosity and zero thermal conductivity we get:

$$\frac{D\rho}{Dt} = -\rho \nabla \cdot \vec{u} \tag{37}$$

$$\rho \frac{D\vec{u}}{Dt} = -\nabla p + \rho \vec{f} \tag{38}$$

$$\rho \frac{De}{Dt} = -p \nabla \cdot \vec{u} \tag{39}$$

The German Ludwig Prandtl presented in 1904 a study, where he showed that the flow around a body can be modelled by two different areas. He proved that the viscous effects can be modelled by dividing the flow field into two layers. The boundary layer, dominated by viscosity, and a layer outside of the boundary layer where viscosity effects can be neglected without any significant errors in the solution. He therefore proved the usefulness of the Euler equations. In the scope of this study, the simulations are based on this approach. (CHRISTODOULOU, 2007; BARDOS, GOLSE, LEVERMORE, 1993)

3. SHOCK WAVES

In subsonic compressible flow, the flow far ahead of the body is forewarned about the presence of the body and adjusts accordingly. In supersonic flow though, the flow upstream of the body only knows about the bodies presence when it encounters the leading-edge shock wave. Every supersonic flow is subject to shock waves and therefore the understanding of shockwaves is of great importance when studying supersonic flow.

Shock-waves are extremely thin regions (10^{-5} cm), where drastic changes in flow properties can occur. Shock waves appear either, in oblique angles to the flow as represented in Figure 3.1, or, in normal angles in relation to the flow as represented in Figure 3.2.

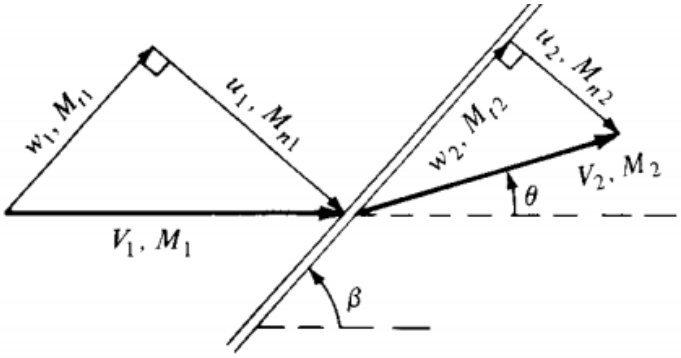

Figure 3.1 Oblique shock extracted from (ANDERSON, 2017)

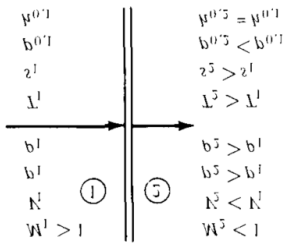

Figure 3.2 Normal shockwave extracted from (ANDERSON, 2017)

According to Anderson (2017) in both cases, an discontinuous increase in pressure is observable across the wave, as an almost explosive compression process occurs. Pressure, temperature, density and entropy increase across the shock while total pressure, velocity and Mach number decrease. Adams (2010) and Anderson (2017) state that the basic normal shock equations for steady, adiabatic, inviscid flow are

$$\rho_1 u_1 = \rho_2 u_2 \tag{40}$$

$$p_1 + \rho_1 u_1^2 = p_2 + \rho_2 u_2^2 \tag{41}$$

$$h_1 + \frac{u_1^2}{2} = h_2 + \frac{u_2^2}{2} \tag{42}$$

Hereby, eq. (40) is the continuity equation, whereas eq.(41) presents the momentum equation and eq.(42) the energy equation. The subscript $_1$ refers to the region bevor and respectively $_2$ to the region behind the shock.

In Figure 3.1 for an oblique shock wave the angle between the wave and the upstream flow direction is defined as the wave angle β and the downstream flow is inclined by the deflection angle θ. The equations above, lead to the relations for changes across a shock wave from the region before and after the wave, at a wave angle $\xi < \beta < \frac{\pi}{2}$, where represents the acoustic limit:

$$\frac{\rho_2}{\rho_1} = \frac{(\gamma+1)M_1^2 \sin^2\beta}{2 + (\gamma+1)M_1^2 \sin^2\beta} \tag{43}$$

$$\frac{p_2}{p_1} = \frac{2\gamma}{\gamma+1} M_1^2 \sin^2\beta - \frac{\gamma-1}{\gamma+1} \tag{44}$$

$$\frac{T_2}{T_1} = \left(\frac{2\gamma}{\gamma+1} M_1^2 \sin^2\beta - \frac{\gamma-1}{\gamma+1}\right)\left(\frac{\gamma-1}{\gamma+1} + \frac{2\gamma}{\gamma+1} M_1^2 \sin^2\beta\right) \tag{45}$$

The Rankine-Hugoniot relation brings the flow in the region before and after the shockwave in relation and establishes an expression for the Mach number in the region behind the shock (M_2):

$$M_2^2 \sin^2(\beta - \theta) = \frac{M_1^2 \sin^2 \beta + \frac{2}{\gamma - 1}}{\frac{2\gamma M_1^2 \sin^2 \beta}{\gamma - 1} - 1} \tag{46}$$

From a physical point of view, the flow across a wave is adiabatic and the total enthalpy is constant across the wave. We can derive from eq. (42) that the flow ahead of the shock has to be supersonic, whereas behind the shock, the flow usually is also supersonic, although special cases exist, where the oblique shock is sufficiently strong to decelerate the flow downstream of the shock to subsonic Mach numbers. For normal shocks, the downstream flow is always subsonic.

4. AERODYNAMIC CENTER

The aerodynamic center (AC) is the point on a lifting surface where the pitching moment remains approximately constant with variation of the angle of attack. The position of the center of gravity (CG) relative to the aerodynamic center is of great importance concerning both the static and dynamic longitudinal stability. A dimensionless distance between the center of gravity and the aerodynamic center with regard to the mean aerodynamic chord ($\bar{c}_W$) of the wing can be defined as a measure of longitudinal stability and is called static margin:

$$\frac{x_{CG}}{\bar{c}_W} - \frac{x_{AC}}{\bar{c}_W} = \bar{x}_{CG} - \bar{x}_{AC}[\%] \tag{47}$$

Where:

x_{AC} = position of the aerodynamic center

x_{CG} = position of the center of gravity

$\bar{c}_W$ = mean aerodynamic chord

This measure is expressed in per cent and for stable aircraft configurations its value is negative. According to Hornung (2015), civil and transport aircraft achieve values between -5% and -10%, whereas new combat aircrafts reach values of up to +15%, as they are designed in an instable way. Figure 4.1 represents two cases of the position of the center of gravity regarding the aerodynamic center. In the first (1) the position of the center

of gravity lies in front of the aerodynamic center causing a positive moment and therefore decreasing the Δα which results in a stable behaviour as Δα increases.

The second case (2) represents an instable behavior, as the center of gravity lies behind the aerodynamic center, which leads to a negative moment as Δα increases and therefore in an increase in Δα. (Hornung, 2015)

A third case, which is not represented in the figure is the case of neutral stability, when CP and AC fall together at the same point. This case represents an indifferent behavior of the airplane with respect to a change in Δα. Depending on the type of aircraft such configurations can be desirable, e.g. for aerobatic aircrafts.

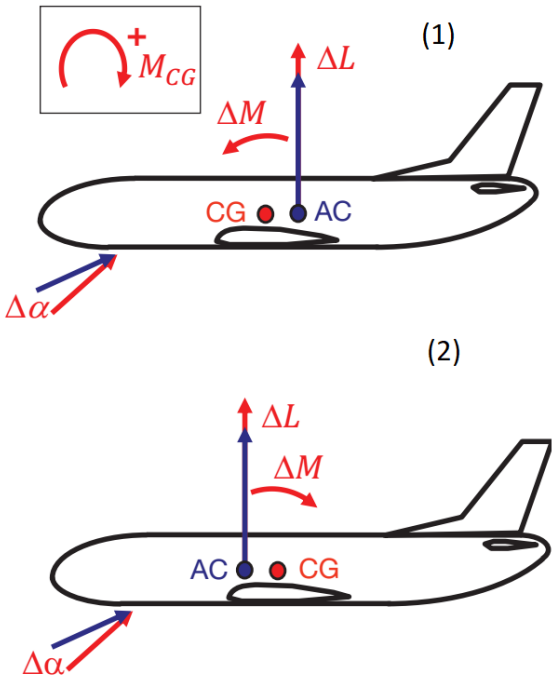

Figure 4.1 Position of the center of gravity and the center of pressure extracted from (HORNUNG, 2015)

Following an approach by Etkin (1996) these statements are going to be deduced theoretically. The aerodynamic forces on lifting surfaces can be represented as lift and

drag acting at the mean aerodynamic center, together with a pitching moment independent of the angle of attack.

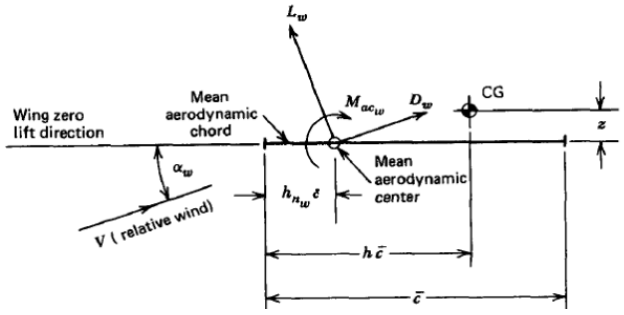

Figure 4.2 Moment about the CG in the plane of symmetry extracted from (ETKIN, 1996)

The position of the center of gravity is from now represented by h, and the position of the aerodynamic center by h_n.

Figure 4.2 shows the total moment for the wing about its CG, which is given by:

$$M_w = M_{ac,w} + (L_w \cos\alpha_w + D_w \sin\alpha_w)(h - h_{n,w})\bar{c} + (L_w \sin\alpha_w - D_w \cos\alpha_w)z \tag{48}$$

In this case the hypothesis of a small angle of attack α is assumed which justifies the sine and cosine approximations ($\cos\alpha_w = 1; \sin\alpha_w = 1$). By dividing eq. (48) by $\frac{1}{2}\rho V^2 S\bar{c}$ it is made nondimensional and becomes:

$$C_{M,w} = C_{Mac,w} + (C_{L,w} + C_{D,w}\alpha_w)(h - h_{n,w}) + (C_{L,w}\alpha_w - C_{D,w})\frac{z}{\bar{c}} \tag{49}$$

Etkin (1996) claims that the last term in eq. ((49) is negligible, and $C_{D,w}\alpha_w$ may also be neglected in comparison with $C_{L,w}$ which leads us to the equation that represents the wing pitching moment:

$$C_{M,w} = C_{Mac,w} + (C_{L,w})(h - h_{n,w}) = C_{Mac,w} + \alpha_w\alpha_w(h - h_{n,w}) \tag{50}$$

The wing is not the only part of an airplane that accounts for a pitching moment. Body and nacelles must be considered as well. Their contribution is quite complex due to interference effects. The body distorts the flow of the wing, and vice versa. If wing, body and nacelles are examined, the same equation as for a wing (eq. (50)) can be used but with different values of the parameters accounting for the usual interpretation of a forward shift of the mean aerodynamic center, the increase in the lift-curve slope, and a negative increment in $C_{Mac,w}$.

$$C_{M,wb} = C_{Mac,wb} + (C_{L,wb})(h - h_{n,wb}) = C_{Mac,wb} + \alpha_{wb}\alpha_{wb}(h - h_{n,wb}) \qquad (51)$$

Here α_{wb} represents the lift-curve-slope of the configuration of wing, body and nacelles. After considering wing, body and nacelles, the tail has also to be examined. It can be represented the same way as an isolated wing, but the occurring interference effects must be considered separately. The most important one is the mean downwash, which stands for the downward deflection of the flow at the tail caused by the wing. Further interference effects are the blanking of part of the tail by the body and the reduction of the relative wind when the tail lies in the wing wake. The forces acting on the tail are visualized in Figure 4.3. The subscript t refers to the tail.

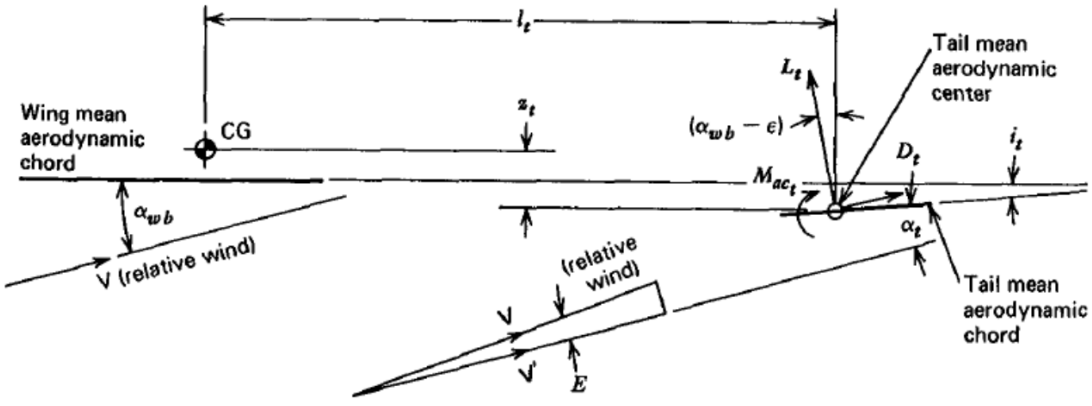

Figure 4.3 Forces acting on the tail of an airplane extracted from (ETKIN, 1996)

The total lift of the airplane is

$$L = \mathrm{L_{wb}} + \mathrm{L_t} \tag{52}$$

and in coefficient form

$$C_L = C_{L,wb} + \frac{S_t}{S} C_{L,t}. \tag{53}$$

$C_{L,t}$ represents the lift coefficient of the tail, based on the dynamic pressure and the tail area S_t.

From this Figure 4.3, we obtain the pitching moment of the tail about the CG:

$$M_t = -l_t[L_t \cos(\alpha_{wb} - \varepsilon) + D_t \sin(\alpha_{wb} - \varepsilon)] - z_t[D_t \cos(\alpha_{wb} - \varepsilon) - L_t \sin(\alpha_{wb} - \varepsilon)] + M_{ac,t} \tag{54}$$

The downwash is characterized by the mean downwash angle ε. According to Etkin (1996), the first term is dominant, while the others can be neglected. In combination with the assumption of small angles this leads us to:

$$M_t = -l_t L_t = -l_t C_{L,t} \frac{1}{2} \rho \mathrm{V}^2 S_t \tag{55}$$

Now, the coefficient form can be obtained

$$C_{M,t} = \frac{l_t}{\bar{c}} \frac{S_t}{S} C_{L,t} = -V_H C_{L,t} \tag{56}$$

In eq.(56), $l_t S_t / S\bar{c}$ represents the ratio of two volumes and is named "horizontal-tail volume ratio" and will be denoted V_H. The center of gravity varies in its position depending on the loading configuration and the fuel consumption, hence V_H is not a constant. Thus, it makes sense to express to define the pitching moment coefficient as a function of the aerodynamic center of the wing-body combination. Using

$\overline{V_H} = \frac{\bar{l}_t}{\bar{c}} \frac{S_t}{S}$ and $V_H = \overline{V_H} - \frac{S_t}{S}(h - h_{n,wb})$

we obtain the moment about the wing-body aerodynamic center

$$\overline{C_{M,t}} = \overline{V_H} C_{L,t} \tag{57}$$

and the moment about the CG:

$$C_{M,t} = -\overline{V_H} C_{L,t} + \frac{S_t}{S}(h - h_{n,wb}) C_{L,t} \tag{58}$$

For the consideration of the propulsive system two parts have a contribution, namely forces cause by the propulsion system itself and the interference effects of the propulsive stream with other aircraft parts. Etkin (1996) makes the assumption that the interference part is already included in the moments for wing, body and tail and the propulsion effects can be represented by $C_{M,p}$.

Summing up the coefficients for the wing-body-nacelle combination (eq.(51)), the coefficient of the tail (eq.(58)), the coefficient accounting for the propulsive system, and using eq.(53) we get the total pitching moment about the CG:

$$C_M = C_{Mac,wb} + C_L(h - h_{n,wb}) - \overline{V_H} C_{L,t} + C_{M,p} \tag{59}$$

To obtain the pitch stiffness ($-C_{M,\alpha}$) eq. (57) is differentiated with respect to α:

$$C_{M,\alpha} = \frac{\partial C_{Mac,cb}}{\partial \alpha} + C_{L,\alpha}(h - h_{n,wb}) - \overline{V_H} \frac{\partial C_{L,t}}{\partial \alpha} + \frac{\partial C_{M,p}}{\partial \alpha} \tag{60}$$

According to the definition of the mean aerodynamic center at the beginning of this chapter, the term $\frac{\partial C_{Mac,cb}}{\partial \alpha}$ is equal to zero, which leads to

$$C_{M,\alpha} = C_{L,\alpha}(h - h_{n,wb}) - \overline{V_H} \frac{\partial C_{L,t}}{\partial \alpha} + \frac{\partial C_{M,p}}{\partial \alpha} \tag{61}$$

As the value of $C_{L,\alpha}$ is large with respect to the other values of the $C_{M,\alpha}$, $C_{M,\alpha}$ depends strongly on the value of h. We define a position of the CG for which $C_{M,\alpha}$ is zero. This represents the boundary between the positive and negative stiffness and can therefore be defined as the neutral point or the aerodynamic center of the whole aircraft. Its location is given by setting eq. (58) equal to zero, which leads to:

$$h_n = h_{n,wb} - \frac{1}{C_{L,\alpha}}\left(\frac{\partial c_{Mac,cb}}{\partial \alpha} - \overline{V_H}\frac{\partial c_{L,t}}{\partial \alpha} + \frac{\partial c_{M,p}}{\partial \alpha}\right) \tag{62}$$

Substituting this expression back into equation (58) we are presented with the simplified expression:

$$C_{M,\alpha} = C_{L,\alpha}(h - h_n) = -C_{L,\alpha}K_n \tag{63}$$

where

$$K_n = (h - h_n) \tag{64}$$

The criterion to be satisfied for static stability is $C_{M,\alpha} < 0$, which represents positive stiffness, then $K_n > 0$, or $h < h_n$. This leads us to the same conclusion as was already obtained from HORNUNG at the very beginning and is represented in (eq. 47):

For static stability, the CG must be forward of the aerodynamic center.

For subsonic flow, the aerodynamic center is located at the 25% chord. When examining supersonic flows, a shift from the 25% chord to the 50% chord is observed. This is denoted the aerodynamic center shift. A detailed knowledge of the aerodynamic center position and its shift in the transonic regime is a very important factor, in order to minimize trim drag, maximize load-factor capability, and provide acceptable handling qualities. (ETKIN, 1996; HORNUNG, 2015)

5. THE ADJOINT METHOD

The adjoint method is a method that has been broadly studied and used as an aircraft design tool. CFD-based aerodynamic optimization requires a very large number of design parameters and a reasonable calculation effort. Due to the resulting computational effort, the possibility of allowing many parameters to be varied is questionable with conventional methods. Using the adjoint method, sensitivities (derivations) of flow quantities and quantities derived therefrom can be calculated according to geometric parameters. This is significantly more efficient than the calculation of derivatives by means of flow solutions, e.g. by finite differences when many parameters and relatively few target variables are considered. Since only one adjoint solution has to be calculated for each functional, the effort for a sensitivity calculation of target variables is independent of the number of design parameters and a powerful acceleration in computing speed is obtained. This improves optimization significantly as the number of equations to be solved is independent of the number of design parameters.

The adjoint method, based on the control theory of systems governed by differential equations, was initially proposed by Pironneau for shape optimization in elliptical problems and later extended for transonic flows by Jameson. The traditional approach by Jameson will be presented in a summarized version in the following.

5.1 FORMULATION OF THE ADJOINT METHOD

According to Hayashi (2016) in aerodynamic applications, relevant measures of merit, I, normally involve functions of flow variables, $\boldsymbol{Q}$, and the geometry of the solid body surface, G, which can be represented as:

$$I[\boldsymbol{Q}, P] = \int_x F[Q(x), P(x), x]\, dx \tag{65}$$

Here, the vector Q represents the coordinates of the analyzed system in the space of state. The vector x represents the coordinates of the domain in physical state, and P encompasses the control parameteres of the system, e.g. the given geometry of a solid body.

The sensitivity of the measure of merit to geometric variations is measured by the Gâteaux differential, which is given by:

$$\delta I = \langle F'_{\boldsymbol{Q}}, \delta \boldsymbol{Q} \rangle + \langle F'_P, \delta P \rangle = \delta I_{\boldsymbol{Q}} + \delta I_P \tag{66}$$

where the first term of the RHS, $\delta I_{\boldsymbol{Q}}$, corresponds to physical variations $\delta \boldsymbol{Q}(x)$ of the total variationδI , whereas the second term, δI_P, is related to the parametric part of the total variation.

The adjoint method intends to restrict the variations of $\delta \boldsymbol{Q}$ to the space of solutions within the space of realizability in order to greatly reduce the computational effort when computing the sensitivity of the measure of merit, δI. Therefore, the adjoint method relies on concepts of the control theory to impose the governing flow equations as constraints to the variational formulation, and thus avoiding non-realizable variations. Assuming that the equations that govern the flow are composed of a system N of K nonlinear PDE's, which are subject to a set of B boundary conditions, imposed on appropriate boundaries, we get:

$$\boldsymbol{N}[\boldsymbol{Q}(x), \mathrm{P}\,] = \boldsymbol{R}\,(x, P) \tag{67}$$

$$\boldsymbol{B}[\boldsymbol{Q}(x)]_s = 0 \tag{68}$$

By introducing the governing equations and its boundary conditions to the original measure of merit, I, by means of the Lagrange multipliers Ψ and Φ, an augmented function G that describes the constrained variational problem can be defined as:

$$G(\boldsymbol{Q}, P, \Phi, \Psi) = \mathrm{I}[\boldsymbol{Q}, P] - \langle \Phi, \mathbf{N} - \mathbf{R} \rangle \tag{69}$$

According to Jameson (JAMESON, 1988) the sensitivity and the variation of the measure of merit can be simplified through transformations to:

$$\delta G = \langle {F'}_P, \delta P \rangle + \langle \Phi, ({\boldsymbol{R}'}_P - {\boldsymbol{N}'}_P)\delta P \rangle \tag{70}$$

in a way that Φ is calibrated to satisfy the adjoint equation:

$$\boldsymbol{N}'^{\times}_{\boldsymbol{Q}} \Phi = {F'}_{\boldsymbol{Q}} \tag{71}$$

where $(\,)^{\times}$ indicates the conjugate transpose, also known as the adjoint matrix.

It can be observed that the gradient accuracy obtained by the adjoint method does not depend on the magnitude of any variation of the parameters δP as it would be the case in when using the finite difference method. The expression δG in eq. (70) is clearly independent of physical variations δQ. Therefore, it is possible to obtain the gradient information without the need for additional flow simulations, which is the essence of the adjoint method as proposed by Jameson for transonic flows. (JAMESON, 1988; HAYASHI, 2016)

6. METHODOLOGY

The first stage of this work was to carry out flow simulations over the airfoils NACA 0012 and RAE 2822 using the previously described Euler equations, plus the ideal gas law. Those equations are discretized, that is, the derivatives are approximated by differences, and then iterated until the residuals reach an appropriate accuracy level. The NACA 0012 is a symmetrical 2-D profile without camber, which is represented by the first two digits, and a maximum thickness of 12% of the chord. It is used as a common test case in computational fluid dynamics. Contrary to that, the RAE 2822 is a supercritical transonic airfoil. The airfoil was designed for transonic speeds with the objective of eliminating or weakening shock waves.

The numerical code that simulates the flow is based on the finite volume method, it uses a unstructured mesh with tetrahedral control volumes and was extracted form a dissertation by Hayashi (2016). The type of mesh used, is a mesh with a square format and periodic conditions at the upper and lower borders as shown in Figure 6.1. In all the used meshes the side of the square was defined as 100 times the chord of the airfoils and farfield boundary conditions were implemented at the left and right borders. The meshes were created with the software Gambit

For this study, the hypothesis of inviscid and compressible flow in a transient regime are assumed. The method of Jameson and the Runge-Kutta five-step method for finite volume solutions are used for the simulation. The chosen convergence criterion (residual) is 10^{-12} and must be reached by the following parameters of the flow: conservation of mass, conservation of energy and the amount of movement in the x and in the y direction.

The boundary conditions of the flow are the free stream conditions of pressure, Mach number, temperature and angle of attack. The pressure and temperature adopted for all flows as a farfield initial state are:

- p_{ff} = 108.988 kPa;
- T_{ff} = 255.55 K.

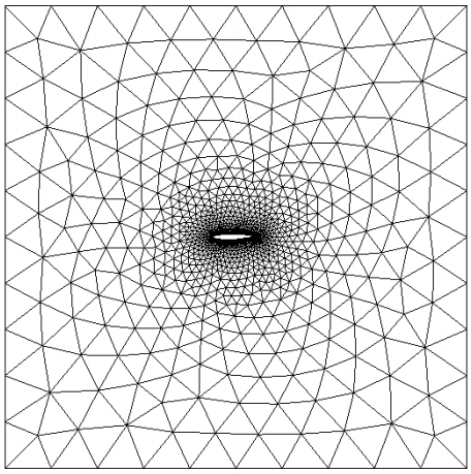

Figure 6.1 Mesh with periodic conditions on the upper and lower border extracted from (HAYASHI, 2016)

The angle of attack and the Mach number are varied for the different simulations. The Euler flow simulations were conducted for Mach numbers between 0.60 and 0.95 Mach for the NACA 0012 airfoil, whereas Mach numbers between 0.60 and 1.00 Mach were chosen for the RAE 2822. For the angle of attack, values from $\alpha = 0°$ to $\alpha = 5°$ for RAE 2822, and angles from $\alpha = 0°$ to $\alpha = 4°$ for NACA 0012 were investigated.

The results of the simulations are obtained in a .vtk file and can be post-processed in data analysis and visualization software. The tools chosen for this study are ParaView and MATLAB. ParaView, due to its flexibility, allowing to visualize distributions of various parameters like density, pressure, temperature and the velocity and MATLAB for the analysis of the obtained data. The results are presented in their dimensionless form in relation to a reference state.

Using the results of the Euler simulations, the values of lift, drag and the moment about the leading edge for the respective angles of attack and Mach numbers were calculated and graphically represented. Dimensional values can be obtained by rearranging the following equations, where ( )* represents the dimensionless values:

- Dimensionless density

$$\rho^* = \frac{\rho}{\rho_{ref}} \tag{72}$$

- Dimensionless velocity

$$u^* = \frac{u}{c_{ref}} \; ; \; v^* = \frac{v}{c_{ref}} \tag{73}$$

- Dimensionless pressure

$$u^* = \frac{u}{\rho_{ref} c_{ref}^2} \tag{74}$$

- Dimensionless temperature

$$T^* = \frac{T}{T_{ref}} \tag{75}$$

This specified reference state is:

- ρ_{ref} = 1.486 kg/m^3
- T_{ref} = 357.78 K
- c_{ref} = 320.44 m/s

To verify and analyze the solutions, MATLAB was used to calculate the pressure coefficient c_p and the critical pressure coefficient $c_{p,crit}$:

$$c_p = \frac{2}{\gamma M_\infty^2}\left\{\frac{p}{p_\infty} - 1\right\} \tag{76}$$

$$c_{p,crit} = \frac{2}{\gamma M_\infty^2}\left\{\left(\frac{1+((\gamma-1)/2)M_\infty^2}{1+(\frac{\gamma-1}{2})}\right)^{\frac{\gamma}{\gamma-1}} - 1\right\} \tag{77}$$

The equilibrium of moments at the leading-edge leads to a linear system from which the position of the aerodynamic center (x_{ac}, z_{ac}) and the moment about the aerodynamic center (M_{ac}) can be obtained, in order to evaluate their evolution with increasing Mach number. For small angles of attack the effect of the drag can be neglected, due to its small values and its negligible lever arm. For each Mach number three different angles of attack are required to determine the linear system with its three unknown variables (x_{ac}, z_{ac}, M_{ac}). The linear system to be solved, is presented in the following:

$$\begin{aligned} M_1 &= L_1 \cos\alpha_1\, x_{ac} + L_1 \sin\alpha_1\, z_{ac} + M_{ac} \\ M_2 &= L_2 \cos\alpha_2\, x_{ac} + L_2 \sin\alpha_2\, z_{ac} + M_{ac} \\ M_3 &= L_3 \cos\alpha_3\, x_{ac} + L_3 \sin\alpha_3\, z_{ac} + M_{ac} \end{aligned} \tag{78}$$

Where:

M_i = Moment about the leading-edge

L_i = Lift

α_i = Angle of attack

x_{ac} = Position of the aerodynamic center on the x-axis in relation to the airfoil chord length

z_{ac} = Position of the aerodynamic center on the z-axis in relation to the airfoil chord length

M_{ac} = Moment about the aerodynamic center

The second stage of this work was to use the results, obtained as described in the section before, as an input for a numerical simulation based on the adjoint method. The codes

extracted from Hayashi (2016) solve the adjoint equations and provide a result, which allows the calculation of sensitivity gradients for the respective measures of merit. In this study, the measures of merit are the lift, drag and the moment about the leading edge. The obtained gradients are with respect to stagnation temperature (T_0) and stagnation pressure (p_0).

The focus of the study is to investigate the influence of compressibility on the aerodynamic center in the transonic region. Therefore, the linear system (78) is derived with respect to stagnation temperature (T_0) and stagnation pressure (p_0). Then, the sensitivity gradients of the lift and the moment about the leading edge, extracted from the numerical simulations, are used to determine the sensitivities of the position of the aerodynamic center and the moment about the aerodynamic center. First, the behavior of the aerodynamic center with respect to the T_0 ($\frac{\partial x_{ac}}{\partial T_0}, \frac{\partial z_{ac}}{\partial T_0}, \frac{\partial M_{ac}}{\partial T_0}$) is investigated solving the linear system (79). Second, the sensitivities of the aerodynamic center with respect to p_0 ($\frac{\partial x_{ac}}{\partial p_0}, \frac{\partial z_{ac}}{\partial p_0}, \frac{\partial M_{ac}}{\partial p_0}$) are investigated solving the linear system (80).

$$\frac{\partial M_1}{\partial T_0} = \cos\alpha_1 \left[\frac{\partial L_1}{\partial T_0} x_{ac} + L_1 \frac{\partial x_{ac}}{\partial T_0}\right] + \sin\alpha_1 \left[\frac{\partial L_1}{\partial T_0} z_{ac} + L_1 \frac{\partial z_{ac}}{\partial T_0}\right] + \frac{\partial M_{ac}}{\partial T_0}$$

$$\frac{\partial M_2}{\partial T_0} = \cos\alpha_2 \left[\frac{\partial L_2}{\partial T_0} x_{ac} + L_2 \frac{\partial x_{ac}}{\partial T_0}\right] + \sin\alpha_2 \left[\frac{\partial L_2}{\partial T_0} z_{ac} + L_2 \frac{\partial z_{ac}}{\partial T_0}\right] + \frac{\partial M_{ac}}{\partial T_0} \qquad (79)$$

$$\frac{\partial M_3}{\partial T_0} = \cos\alpha_i \left[\frac{\partial L_3}{\partial T_0} x_{ac} + L_3 \frac{\partial x_{ac}}{\partial T_0}\right] + \sin\alpha_3 \left[\frac{\partial L_3}{\partial T_0} z_{ac} + L_3 \frac{\partial z_{ac}}{\partial T_0}\right] + \frac{\partial M_{ac}}{\partial T_0}$$

$$\frac{\partial M_1}{\partial P_0} = \cos\alpha_1 \left[\frac{\partial L_1}{\partial P_0} x_{ac} + L_1 \frac{\partial x_{ac}}{\partial P_0}\right] + \sin\alpha_1 \left[\frac{\partial L_1}{\partial P_0} z_{ac} + L_1 \frac{\partial z_{ac}}{\partial P_0}\right] + \frac{\partial M_{ac}}{\partial P_0}$$

$$\frac{\partial M_2}{\partial P_0} = \cos\alpha_2 \left[\frac{\partial L_2}{\partial P_0} x_{ac} + L_2 \frac{\partial x_{ac}}{\partial P_0}\right] + \sin\alpha_2 \left[\frac{\partial L_2}{\partial P_0} z_{ac} + L_2 \frac{\partial z_{ac}}{\partial P_0}\right] + \frac{\partial M_{ac}}{\partial P_0}$$

$$\frac{\partial M_3}{\partial P_0} = \cos\alpha_3 \left[\frac{\partial L_3}{\partial P_0} x_{ac} + L_3 \frac{\partial x_{ac}}{\partial P_0}\right] + \sin\alpha_3 \left[\frac{\partial L_3}{\partial P_0} z_{ac} + L_3 \frac{\partial z_{ac}}{\partial P_0}\right] + \frac{\partial M_{ac}}{\partial P_0} \quad (80)$$

7. RESULTS

7.1.1. EULER FLOW SIMULATION RESULTS

Using the above described numerical codes, the flow over the airfoils NACA 0012 and RAE 2822 was simulated. Their respective geometries are plotted in figures below.

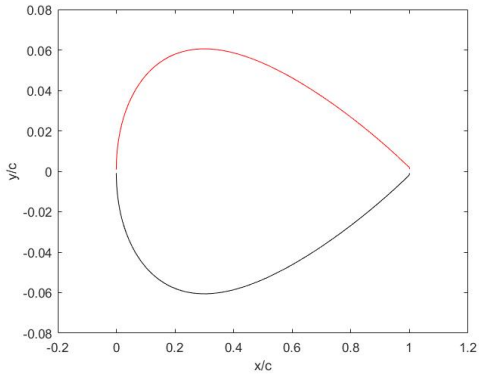

Figure 7.1 NACA 0012 airfoil geometry

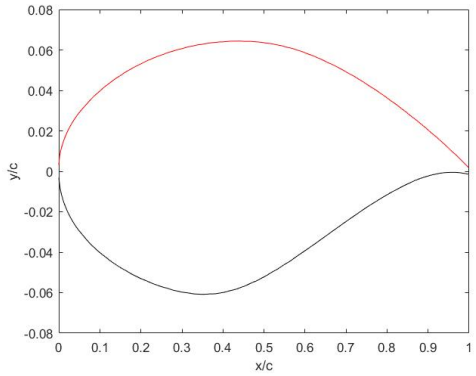

Figure 7.2 RAE 2822 airfoil geometry

The flow simulations over the NACA 0012 airfoil and the RAE 2822 airfoil are presented for angles of attack of $\alpha = 0.0°$, $\alpha = 2.0°$ and free stream velocities of Ma = 0.60, Ma = 0,80 and Ma = 0,90. They are represented with their respective pressure coefficient plots, which were calculated using MATLAB. The Figure 7.3 to Figure 7.14 show the graphics for the NACA 0012, while the Figure 7.15 to Figure 7.26 illustrate the RAE 2822 airfoil.

The velocities were selected, because they illustrate the transonic regime and display the appearance and development of shockwaves.

The velocity contours show for NACA 0012, at zero angle of attack, a uniform velocity contour for the top and bottom side of the airfoil, which was expected due to its symmetry. In Figure 7.4, Figure 7.6 and Figure 7.8 this uniformity of the pressure distribution for the upper and lower sides of the NACA 0012 airfoil can be observed. For an angle of attack of $\alpha > 0.0°$, the Cp-values on the upper surface are higher than on the lower surface, which

coincides with the theory. The same uniformity is obtained for the pressure and temperature plots which are not presented in this work.

For the RAE 2822 the velocity over the upper surface of the airfoil is higher than the velocity over the lower surface, as can be observed in Figure 7.15, Figure 7.17, Figure 7.21, and Figure 7.23. With increasing Mach number though, the velocities approach each other and the difference diminishes. For the pressure and temperature, the contrary is the case, and their values are lower on the upper than on the lower side. This is consistent with Bernoulli's principle that the pressures will be lower on the upper and higher on the lower side and the velocities accordingly higher, on the upper and lower on the lower side, which validates the presented results. The same phenomenon can be observed for the NACA 0012 at an angle of attack different form zero (uniformity), in this case $\alpha = 2.0°$.

When the velocities approach the transonic regime, the development of normal shock waves is expected. The strength of the shock increases with the increase in Mach number. For this case it reaches its peak at Ma = 0.90, which can be observed in the presented figures for both airfoils (Figure 7.7, Figure 7.13, Figure 7.19, Figure 7.25). It can further be observed that the shock shifts to the aft of the airfoil, as the Mach number increases. The shock waves hereby are formed for the NACA 0012 uniformly for $\alpha = 0.0°$ on the upper and lower side of the airfoil, whereas for the RAE 2822 ($\alpha = 0.0°$, $\alpha = 2.0°$) and NACA 0012 at $\alpha = 2.0°$ the shock appears on the upper camber prior to the lower camber.

A comparison of the values of the maximum Mach number, the minimum pressure and the minimum temperature for both airfoils at the same angle of attack displays a tendency that on the NACA 0012 airfoil, the values of the maximum Mach number is lower, and the minimum pressures and minimum temperatures are higher than on the RAE 2822 airfoil.

Comparing the different angles of attack for the same airfoil, it is noticeable that the difference between the minimum pressure coefficients is quite high at lower Mach numbers. These differences, however, diminish with an increasing free stream velocity

and the values approach each other. This can be observed in Figure 7.27 and Figure 7.28, where the variation of the minimum pressure coefficient with increasing Mach number, as well as the critical pressure coefficient is plotted. It can be noticed, that the minimum pressure depends highly on the angle of attack. The behavior is similar for the angles of attack $\alpha = 0.0°$ and $\alpha = 1.0°$. It increases until Ma = 0.80, then decreases until Ma = 0.90 and starts increasing again until Ma = 0.95. For an angle of attack of $\alpha = 4.0°$ though, the behavior differs quite significantly. Instead of increasing, it decreases continuously until Ma = 0.85, then increases slightly to Ma = 0.9 and decreases again. It is also noticeable that for the highest Mach number evaluated in this study for the NACA 0012 airfoil (Ma = 0.95), all minimum pressures meet at very similar values. Similar observations can be made for the RAE 2822 airfoil. For the angles of attack $\alpha = 0.0°$ and $\alpha = 1.0°$ the behavior is almost equal compared with NACA 0012 and for angles greater than $\alpha = 3.0°$ the plots resemble the plot for $\alpha = 4.0°$ of the NACA airfoil. It is notable though, that the pressure coefficients for all angles evaluated for the RAE 2822 airfoil, in contrary to the NACA 0012 decrease with a similar slope commencing at Ma = 0.8 and end as well at very similar values.

The intersection of the minimum pressure coefficient with the critical pressure plot ($C_{p,crit}$) presents us with an estimation of the critical Mach number for the different angles of attack. For the both airfoils the following is valid: the higher the angle of attack, the earlier the critical Mach number is reached.

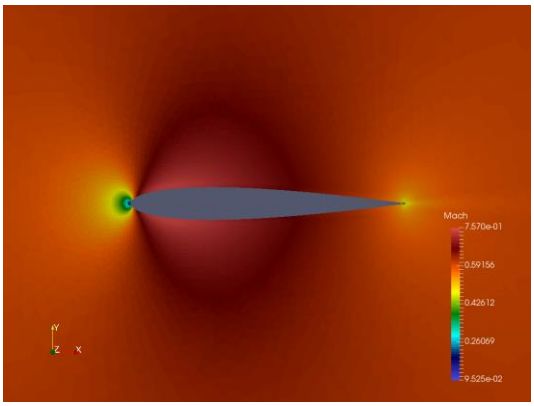

Figure 7.3 Mach number distribution over the NACA 0012 airfoil at a free stream Mach number of Ma = 0.60 and an angle of attack of α = 0.0°

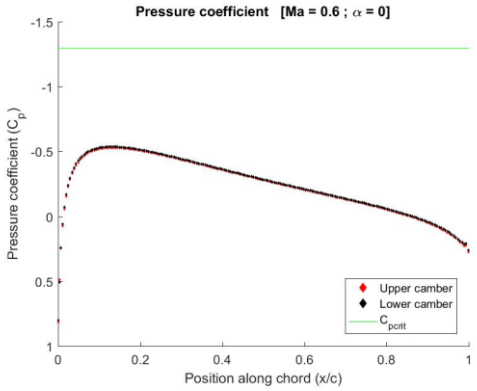

Figure 7.4 Pressure distribution over the NACA 0012 airfoil at a free stream Mach number of Ma = 0.60 and an angle of attack of α = 0.0

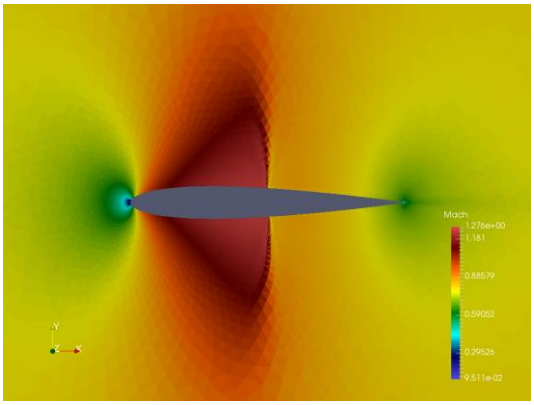

Figure 7.5 Mach number distribution over the NACA 0012 airfoil at a free stream Mach number of Ma = 0.80 and an angle of attack of α = 0.0°

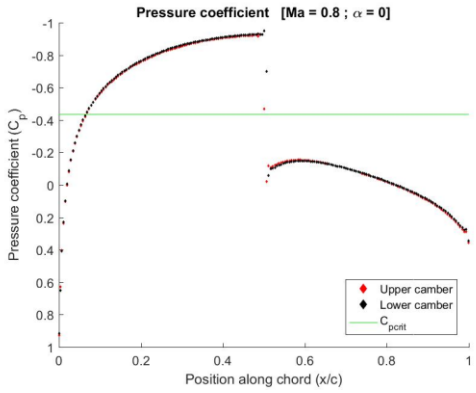

Figure 7.6 Pressure distribution over the NACA 0012 airfoil at a free stream Mach number of Ma = 0.80 and an angle of attack of α = 0.0

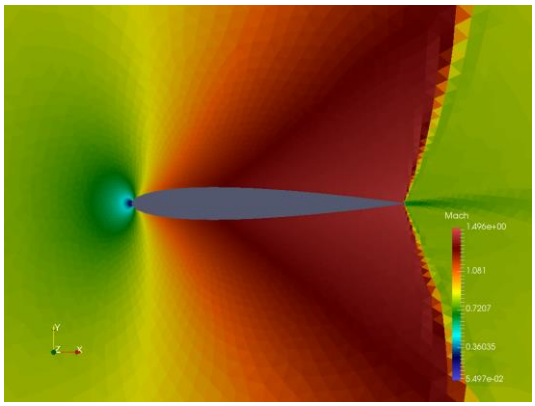

Figure 7.7 Mach number distribution over the NACA 0012 airfoil at a free stream Mach number of Ma = 0.90 and an angle of attack of α = 0.0°

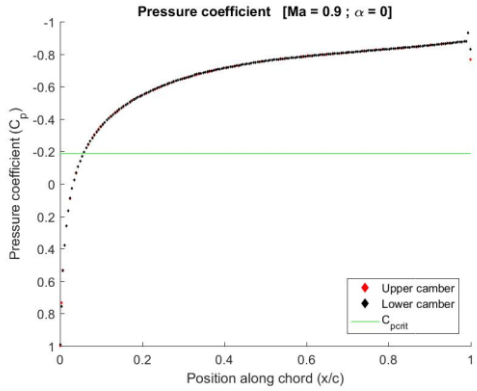

Figure 7.8 Pressure distribution over the NACA 0012 airfoil at a free stream Mach number of Ma = 0.90 and an angle of attack of α = 0.0

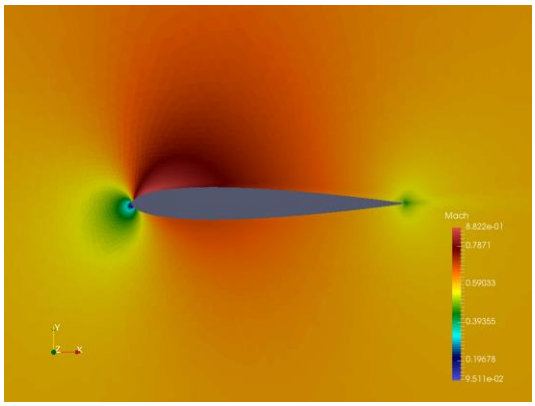

Figure 7.9 Mach number distribution over the NACA 0012 airfoil at a free stream Mach number of Ma = 0.60 and an angle of attack of α = 2.0°

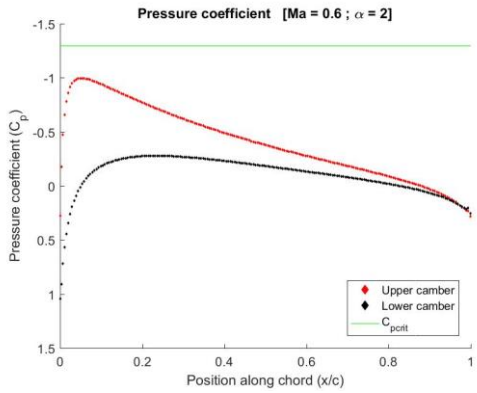

Figure 7.10 Pressure distribution over the NACA 0012 airfoil at a free stream Mach number of Ma = 0.60 and an angle of attack of α = 2.0

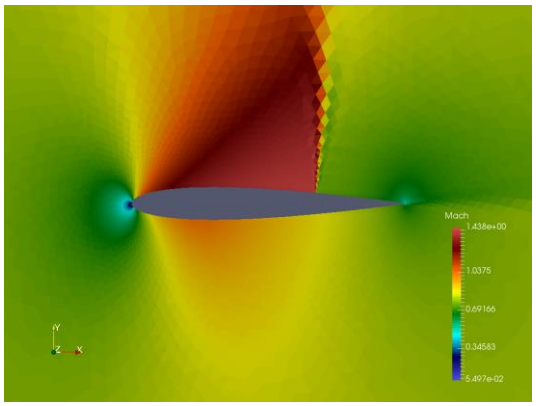

Figure 7.11 Mach number distribution over the NACA 0012 airfoil at a free stream Mach number of Ma = 0.80 and an angle of attack of α = 2.0°

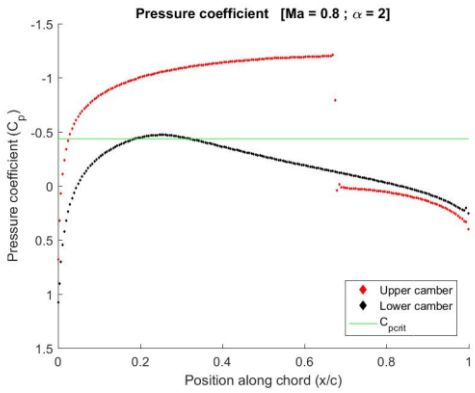

Figure 7.12 Pressure distribution over the NACA 0012 airfoil at a free stream Mach number of Ma = 0.80 and an angle of attack of α = 2.0

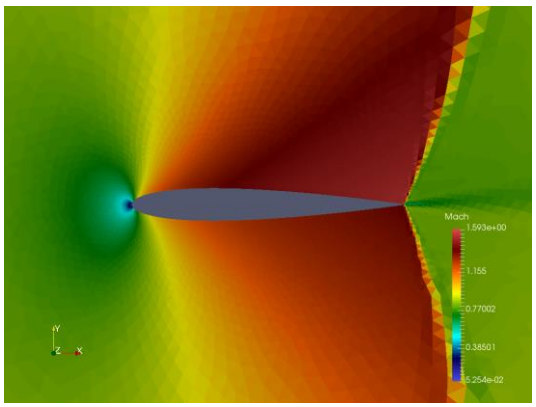

Figure 7.13 Mach number distribution over the NACA 0012 airfoil at a free stream Mach number of Ma = 0.90 and an angle of attack of α = 2.0°

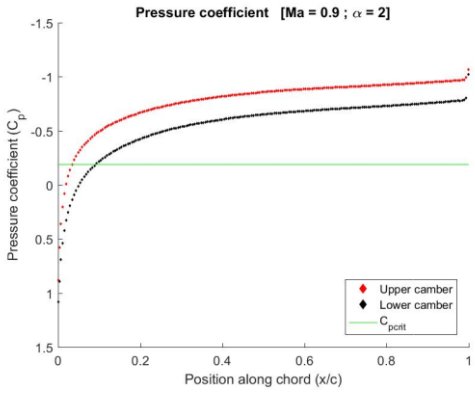

Figure 7.14 Pressure distribution over the NACA 0012 airfoil at a free stream Mach number of Ma = 0.90 and an angle of attack of α = 2.0

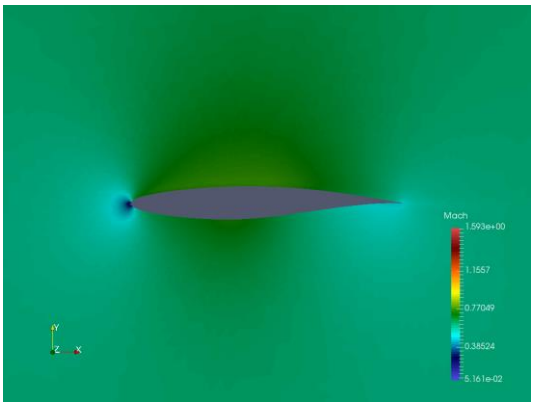

Figure 7.15 Mach number distribution over the RAE 2822 airfoil at a free stream Mach number of Ma = 0.60 and an angle of attack of α = 0.0°

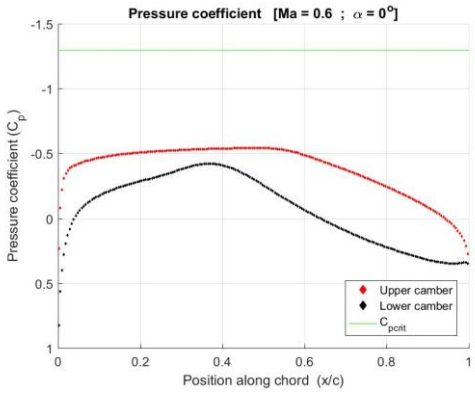

Figure 7.16 Pressure distribution over the RAE 2822 airfoil at a free stream Mach number of Ma = 0.60 and an angle of attack of α = 0.0

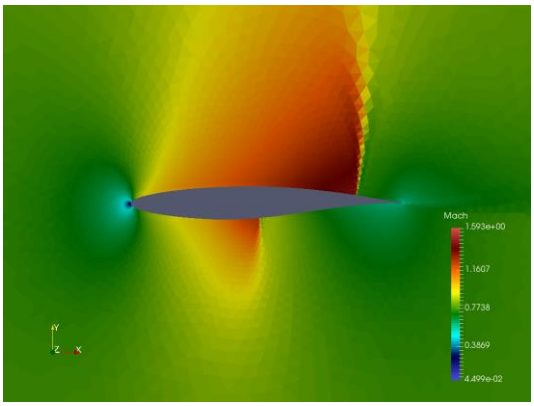

Figure 7.17 Mach number distribution over the RAE 2822 airfoil at a free stream Mach number of Ma = 0.80 and an angle of attack of α = 0.0°

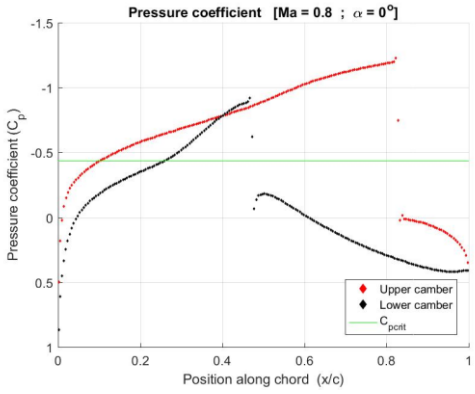

Figure 7.18 Pressure distribution over the RAE 2822 airfoil at a free stream Mach number of Ma = 0.80 and an angle of attack of α = 0.0

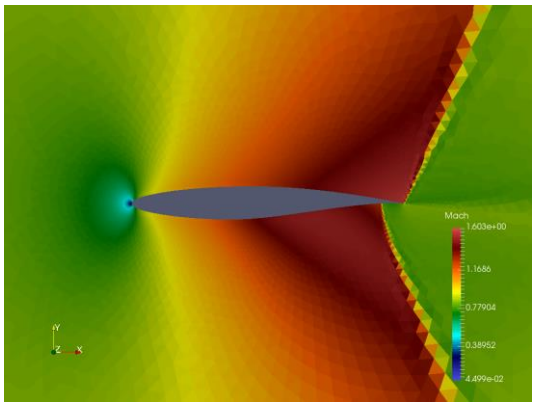

Figure 7.19 Mach number distribution over the RAE 2822 airfoil at a free stream Mach number of Ma = 0.90 and an angle of attack of α = 0.0°

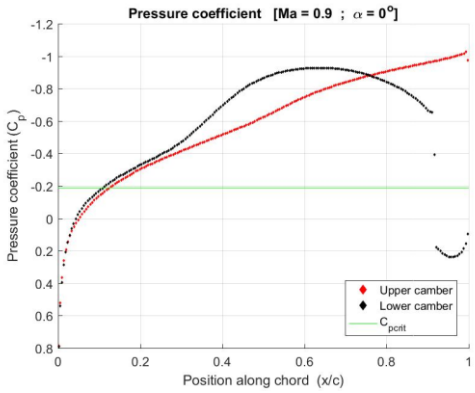

Figure 7.20 Pressure distribution over the RAE 2822 airfoil at a free stream Mach number of Ma = 0.90 and an angle of attack of α = 0.0

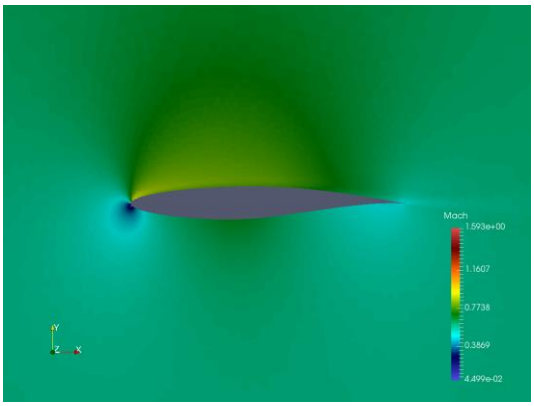

Figure 7.21 Mach number distribution over the RAE 2822 airfoil at a free stream Mach number of Ma = 0.60 and an angle of attack of α = 2.0°

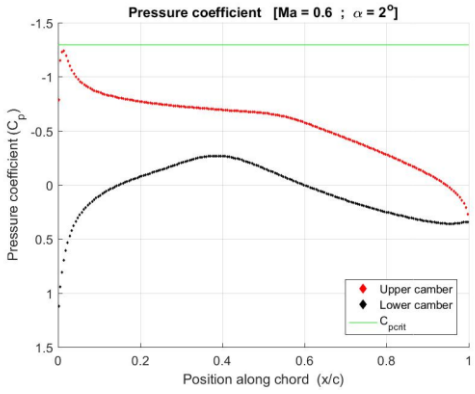

Figure 7.22 Pressure distribution over the RAE 2822 airfoil at a free stream Mach number of Ma = 0.60 and an angle of attack of α = 2.0

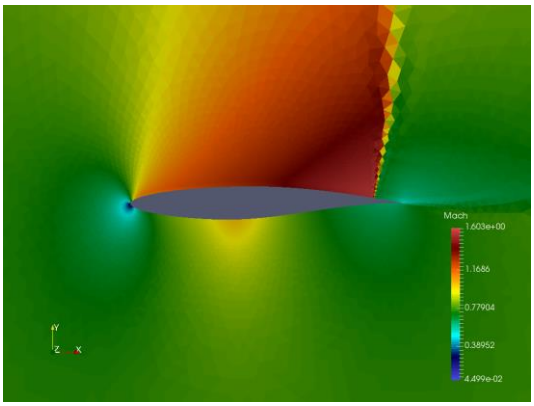

Figure 7.23 Mach number distribution over the RAE 2822 airfoil at a free stream Mach number of Ma = 0.80 and an angle of attack of α = 2.0°

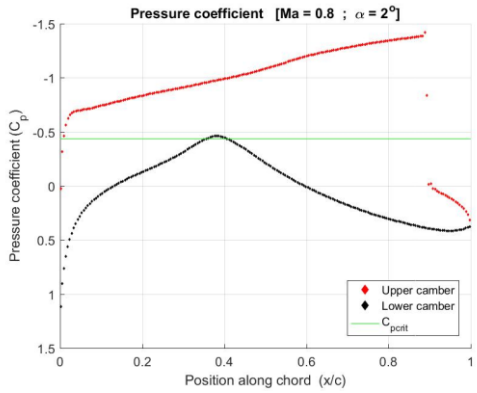

Figure 7.24 Pressure distribution over the RAE 2822 airfoil at a free stream Mach number of Ma = 0.80 and an angle of attack of α = 2.0

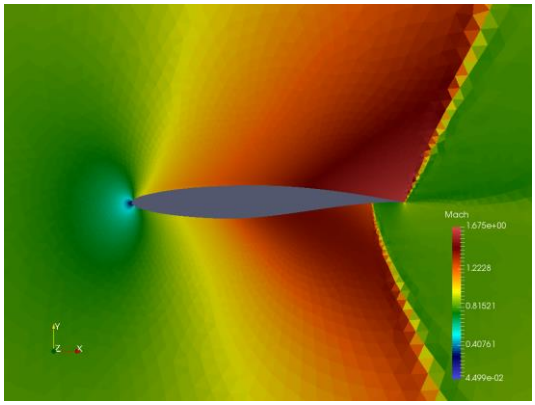

Figure 7.25 Mach number distribution over the RAE 2822 airfoil at a free stream Mach number of Ma = 0.90 and an angle of attack of α = 2.0°

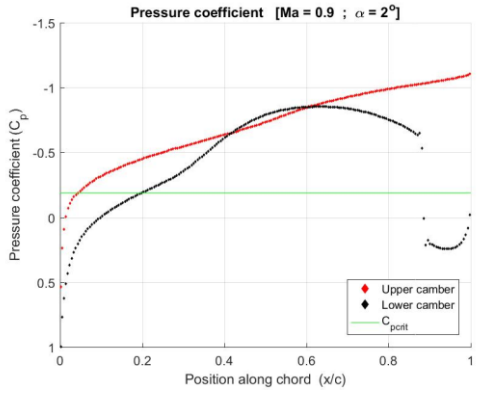

Figure 7.26 Pressure distribution over the RAE 2822 airfoil at a free stream Mach number of Ma = 0.90 and an angle of attack of α = 2.0

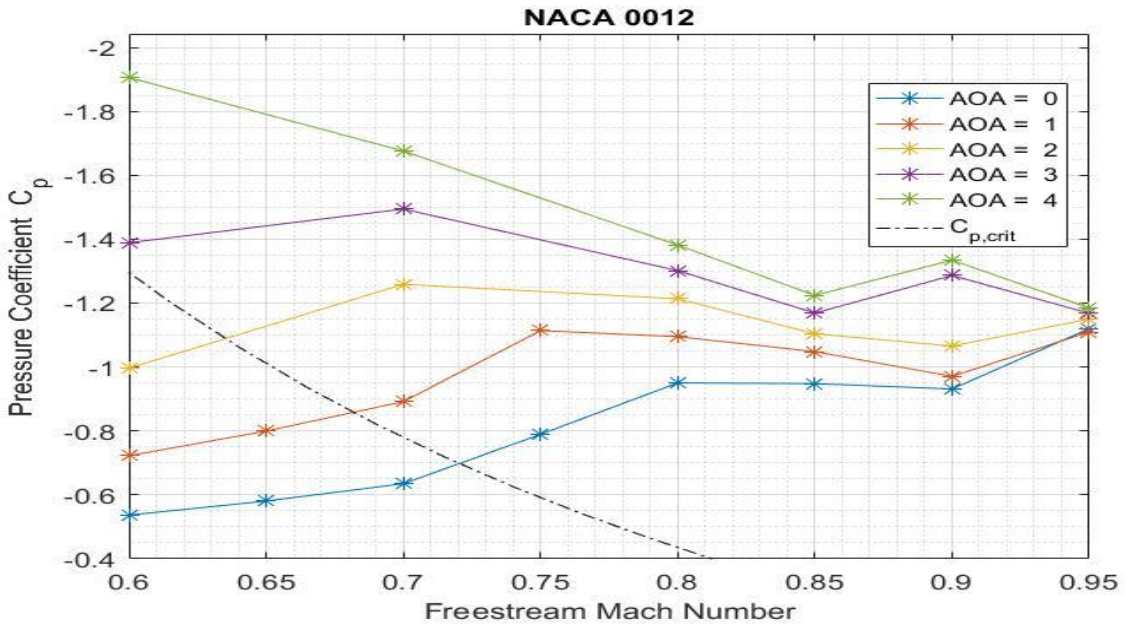

Figure 7.27 Variation of the minimum pressure coefficient $C_{p,min}$ and critical pressure coefficient $C_{p,crit}$ for NACA 0012 with increasing Mach number

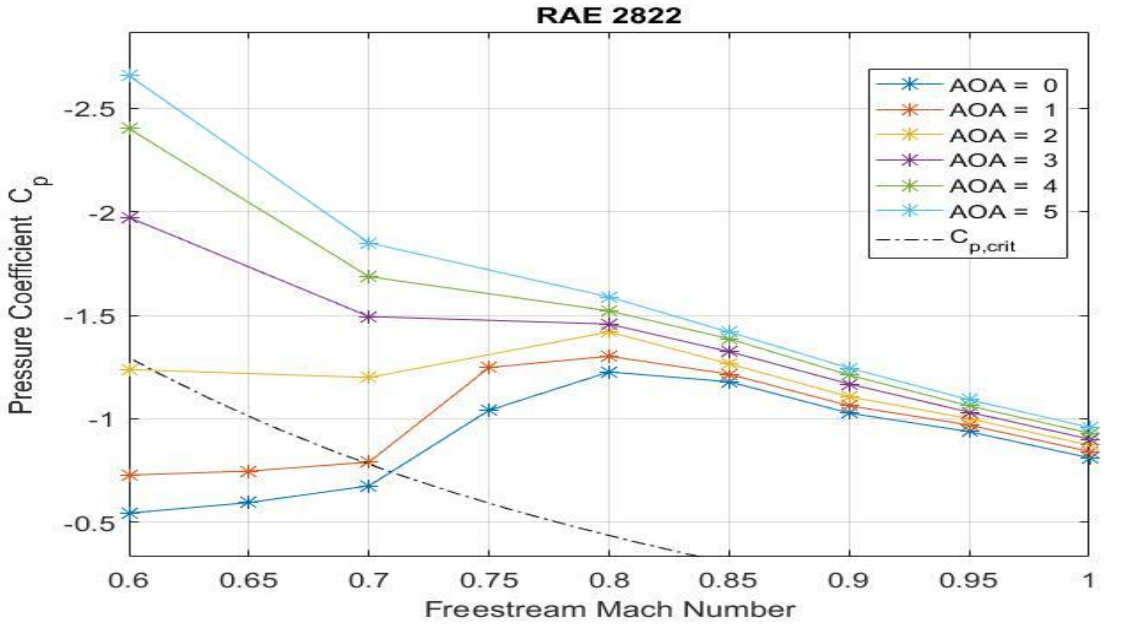

Figure 7.28 Variation of the minimum pressure coefficient $C_{p,min}$ and critical pressure coefficient $C_{p,crit}$ for RAE 2822 with increasing Mach number

The behavior of the wave drag, with augmenting Mach number is displayed in Figure 7.29 for the NACA 0012 airfoil and in Figure 7.30 for the RAE 2822 respectively. All values are presented in their dimensionless form, as they are calculated from the adimensional parameters described in the section 6, Methodology. It is worth to remember, that the adopted model for the flow is inviscid and, therefore only wave drag can be obtained from the solutions.

The behavior of the wave drag and the values for the same Mach number and same angle of attack are very similar for both airfoils. Coinciding with the theory, higher angles of attack lead to higher values of wave drag. A steep increase in drag can be noticed, starting at approximately Ma = 0.70. The drag continues to increase until a velocity of Ma = 0.90, where the curves start to flatten. Consistent with the results presented above and in Figure 1.1, the wave drag starts to increase, when the flow over the airfoil reaches the critical Mach number and therefore supersonic speeds. The appearance of the wave drag starts at a Mach number between Ma = 0.60 and Ma = 0.75. This coincides with the data plotted in Figure 7.27 and Figure 7.28. For a more detailed investigation of the critical Mach number and when exactly the wave drag appears, more simulations have to be conducted, in order to obtain more points in the plots.

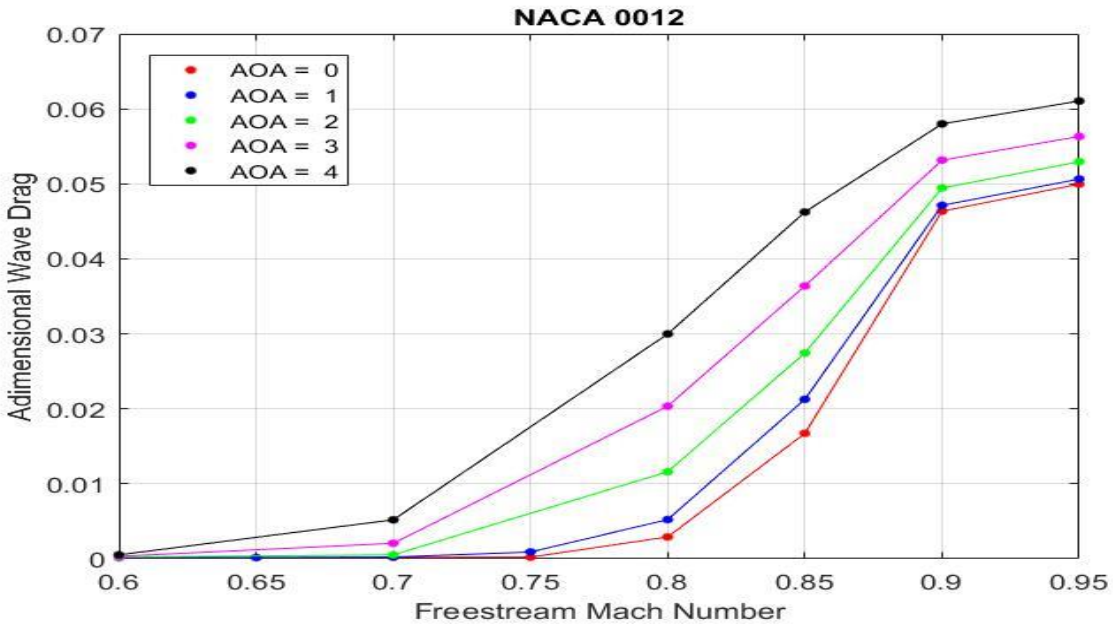

Figure 7.29 Variation of wave drag for the NACA 0012 airfoil with increasing freestream Mach number

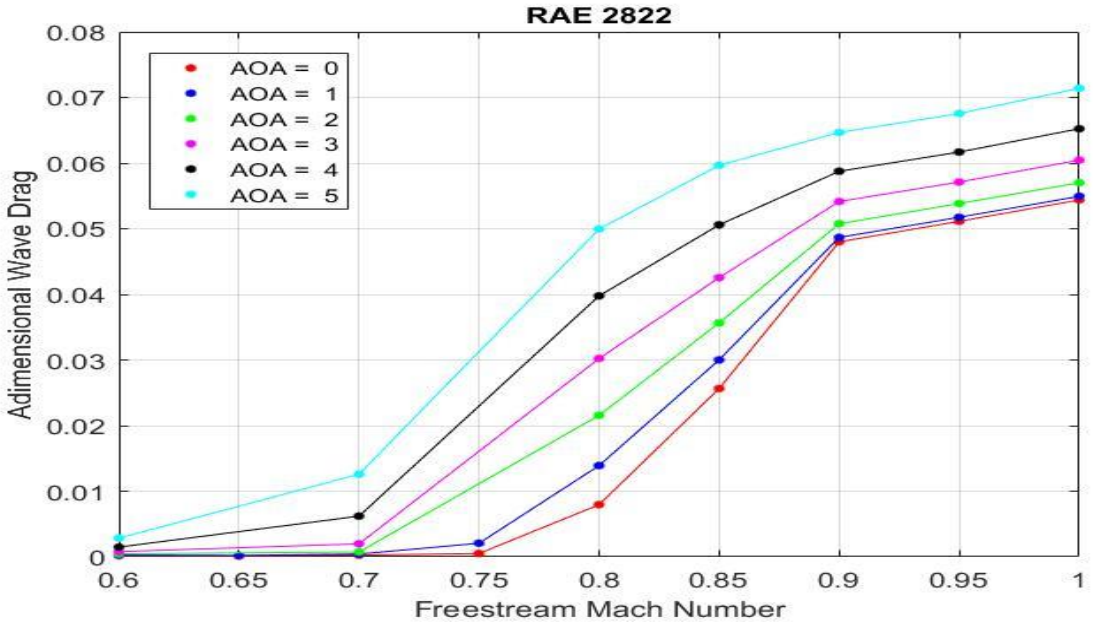

Figure 7.30 Variation of wave drag for the RAE 2822 airfoil with increasing freestream Mach number

For the calculation of the aerodynamic center, pitching moment about the leading edge and lift are needed. The variation of the lift with increasing Mach number is plotted for NACA 0012 and RAE 2822 in Figure 7.31 and Figure 7.32. The behavior of the two airfoils is very similar. As expected, no lift is generated for the NACA 0012 at a zero angle of attack, although at Ma = 0.85 a small amplitude is noticeable. For the other angles of attack as well as for the RAE 2822 airfoil it can be observed, that the lift starts increasing in the region where the critical Mach number is reached. For the NACA 0012 the lift keeps increasing until reaching a peak at a Mach number of Ma = 0.85, where it starts decreasing until Ma = 0.90, from where it almost stabilizes until Ma = 0.95. For the RAE 2822 the behavior is very similar, although it reaches its peak earlier, at Ma = 0.80. This coincides with the pressure coefficient plots. For the plots presented above it can be seen that the greatest pressure difference between the upper and lower side of the airfoil exists for Ma = 0.80, which results in a greater lift generation. The comparison of the two graphics shows a predominance of the airfoil geometry until the respective peaks are reached. The lift values are hereby higher for the RAE 2822 than for the NACA 0012, but both drop to similar values after the peak.

The behavior of the pitching moment about the leading edge with increasing Mach number is plotted in Figure 7.33 for the NACA 0012 airfoil and in Figure 7.34 for the RAE 2822 airfoil. The pitching moment graph is very similar to the lift graph, only that it is inverted. For both airfoils, instead of increasing, it starts decreasing in the region where the critical Mach number is reached until Ma = 0.85, where it reaches its peak and starts increasing until stabilizing at Ma = 0.90. This behavior was expected as the pitching moment is a function of the lift and therefore greater lift values lead to greater pitching moment values.

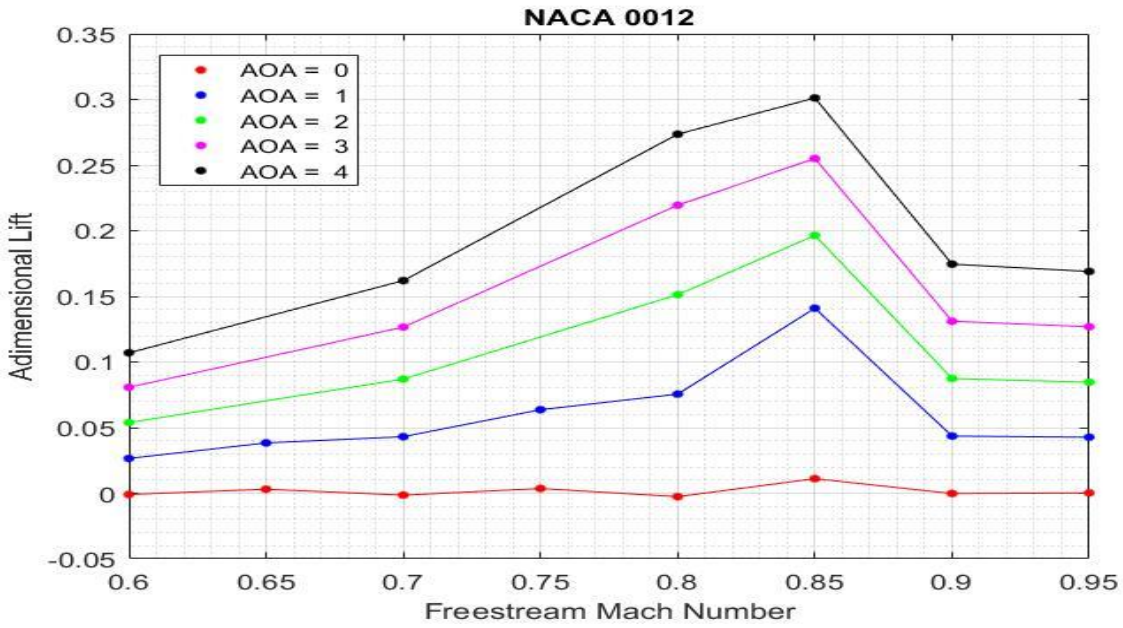

Figure 7.31 Variation of the lift for the NACA 0012 airfoil with increasing freestream Mach number

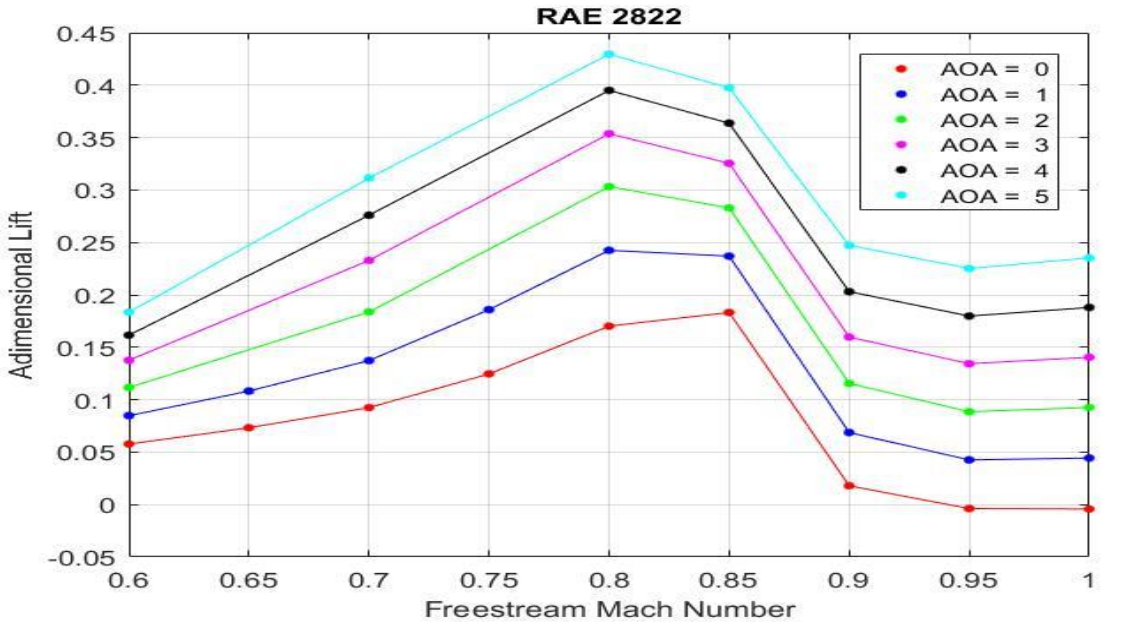

Figure 7.32 Variation of the lift for the RAE 2822 airfoil with increasing freestream Mach number

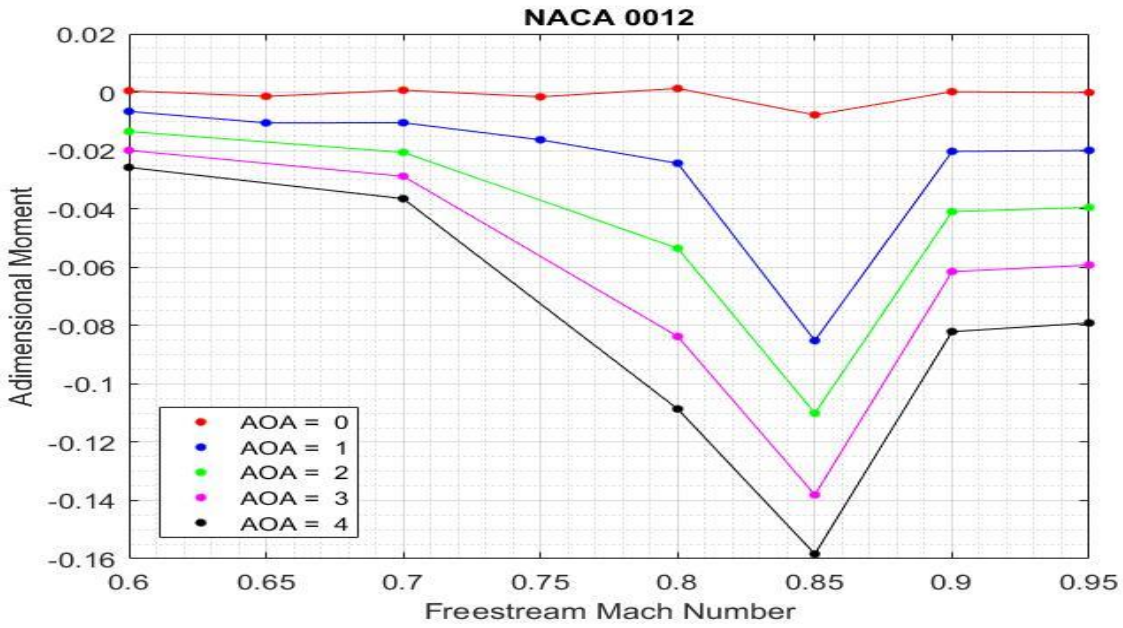

Figure 7.33 Variation of the pitching moment about the leading edge for the NACA 0012 airfoil with increasing Mach number

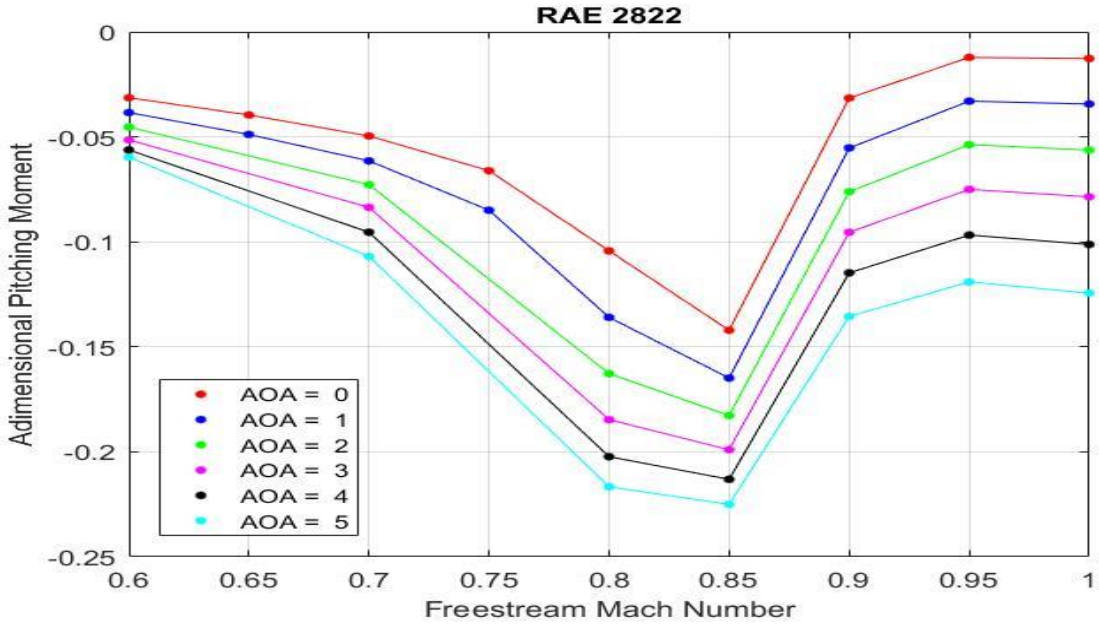

Figure 7.34 Variation of the pitching moment about the leading edge for the RAE 2822 airfoil with increasing Mach number

Now, that all the forces influencing the aerodynamic center according to the model present in the section of the methodology are calculated and presented, the position of the aerodynamic center and the moment about the aerodynamic center can be obtained.

In Figure 7.35 the variation of the x-coordinate of the aerodynamic center (x_{ac}) with increasing freestream Mach number is presented for both airfoils, NACA 0012 and RAE 2822. The respective values of the plots are displayed in Table 1 for the NACA 0012 and in Table 2 for the RAE 2282. The behavior is quite similar for both airfoils. For subsonic freestream velocities, the x-coordinate of the aerodynamic center of the NACA 0012 is closer to the leading edge than for the RAE 2822. For the NACA 0012 airfoil the value at a freestream Mach number Ma = 0.60 is at 26.8% of the chord, whereas for the RAE 2822 it is at 29.6% of the chord. Both values are close to the 25% chord, the value that can be found in the literature and was presented above in the part of the theory of the aerodynamic center. For both airfoils a minor change of x_{ac} can be noticed at Ma = 0.60. It is interesting, that this minor change of x_{ac} for the NACA 0012 is towards the leading edge, while for the RAE 2822 it moves towards the trailing edge. As the Mach number increases, a shift of the aerodynamic center towards 50% of the chord is observed. The shift to the 50% chord occurs much quicker for the RAE 2822 than for the NACA 0012. At Ma = 0.80 the x_{ac} of the NACA 0012 is still at 30.5% of the chord, whereas the x_{ac} of the RAE 2822 already performed a shift to 45.5% of the chord. From Ma = 0.80 to Ma = 0.90 the x_{ac} of the NACA 0012 undergoes an almost linear shift from 30.5% of the chord to 46.9% of the chord. Once the shift towards the trailing edge for both airfoils has taken place, the position of the aerodynamic center stabilizes at the end of the transonic regime. Examining the results closely it can be seen, that for both airfoils, it doesn't stabilize completely but performs a small shift towards the leading edge.

It was expected, that the position of the aerodynamic center shifts from the 25% chord to the 50% chord once supersonic Mach numbers are reached. It is also consistent with the Cp-plots, for the transonic speed Ma = 0.80 presented above (Figure 7.6, Figure 7.12, Figure 7.18, Figure 7.24, Figure 7.27, Figure 7.28). In the mentioned figures, it can be

observed that, while the shock already moved to the aft of the airfoil for the RAE 2822, this shift hasn't been completed yet for the NACA 0012. Therefore, it is plausible that the shift of the aerodynamic center also still hasn't been completed. This observation is consistent with the fact, that the RAE 2822 airfoil is an airfoil developed for transonic speeds and therefore passes through the transonic regime quicker than normal airfoils. This explains why the shift of the x-coordinate of the aerodynamic is already completed at lower Mach numbers than for the NACA 0012 airfoil.

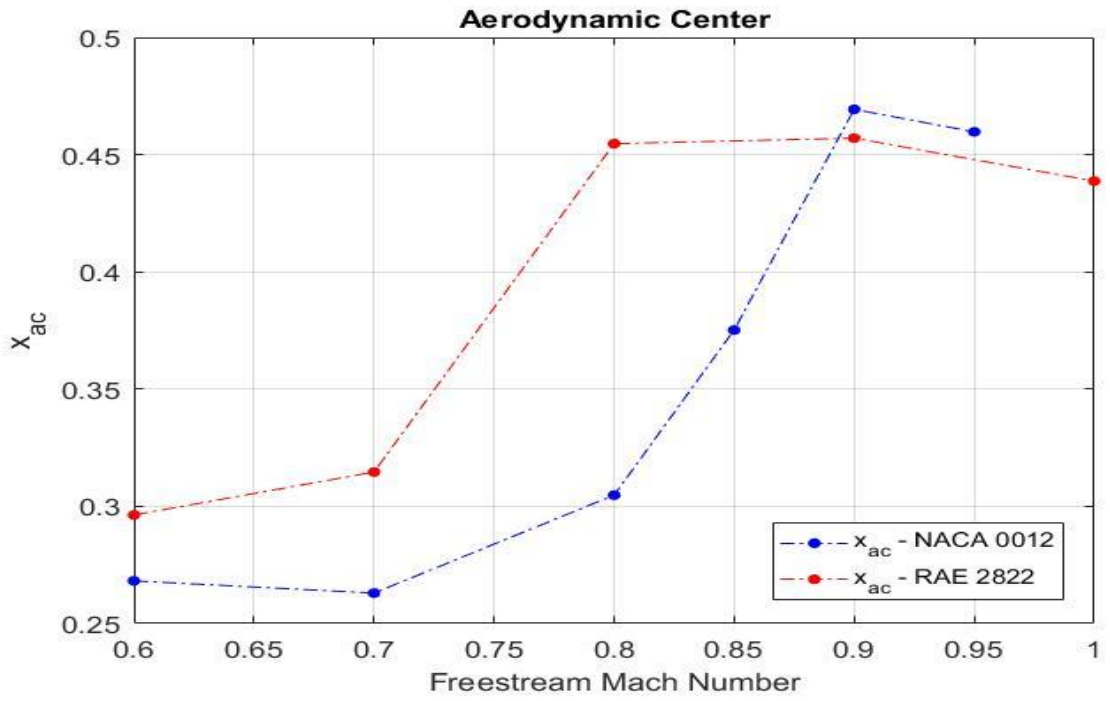

Figure 7.35 Variation of the x-coordinate of the aerodynamic center for the airfoils NACA 0012 and RAE 2822 with increasing free stream Mach number

The variation of the z-coordinate of the aerodynamic center (zac) is represented for both airfoils in Figure 7.36. We notice that the zac of the RAE 2822 starts at a position below the chord at zac = -0.457 for Ma = 0.60 and increases alternatingly to a value of zac = 0.319, which means a position above the chord.It is interesting that the z_{ac} of the NACA 0012 airfoil also varies with increasing Mach number. As it is a symmetric airfoil,

according to theory the z_{ac}, should be located at z = 0. For the presented simulations though this is not the case. In the figure below we can observe according to the results of the simulations the z_{ac} also starts at a position beneath the chord, then shifts to a position way above it, from where it drops to values close to zero. As these results don't coincide with the theory, the results should be treated with caution and further simulations should be conducted, to investigate the phenomenon.

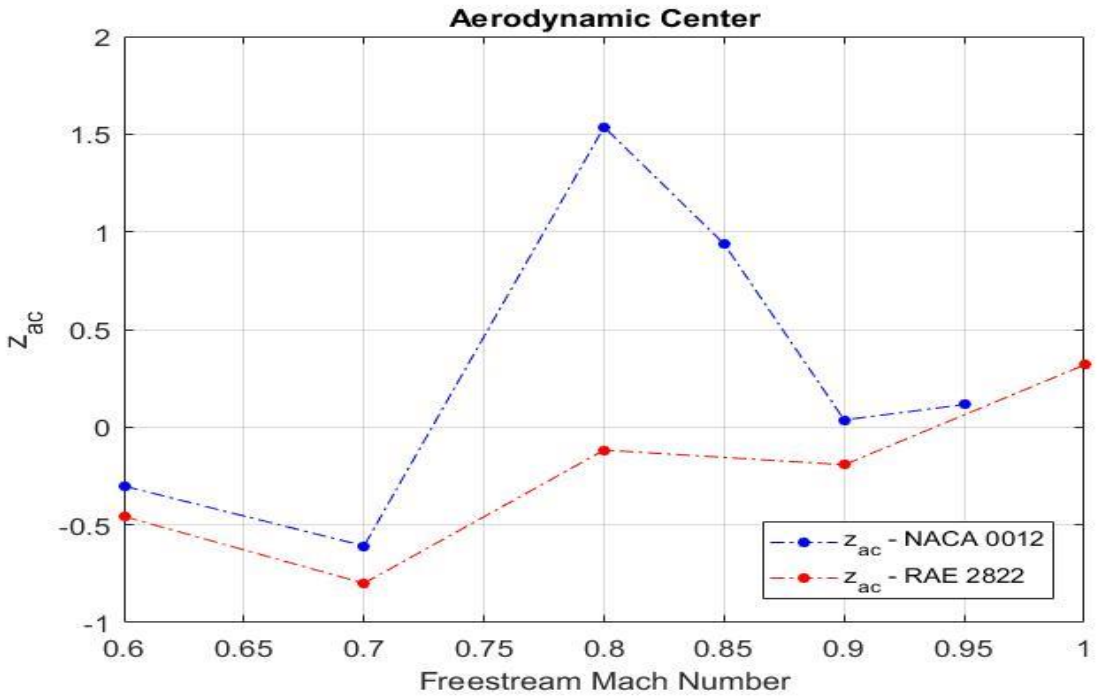

Figure 7.36 Variation of the z-coordinate of the aerodynamic center for the airfoils NACA 0012 and RAE 2822 with increasing free stream Mach number

The last result that is obtained from the Euler flow solutions is the moment about the aerodynamic center (M_{ac}), which is displayed in Figure 7.37. It was expected that its values are going to be zero or close to zero. We can observe, that all the values for the NACA 0012 correspond with the expectations but the value for Ma = 0.85, M_{ac} = 0.030 deviates quite noticeable form zero. This may well be a numerical error that builds up, owing to the instability of the shock wave position at Ma = 0, which is widely

acknowledged in the literature. For the RAE 2822 the behavior is different. A moment about the aerodynamic center is already present, although with a small value at Ma = 0.60. From this point it increases until Ma = 0.80 from where it drops again to a value at Ma = 0, which is similar to the value at Ma = 0.60.

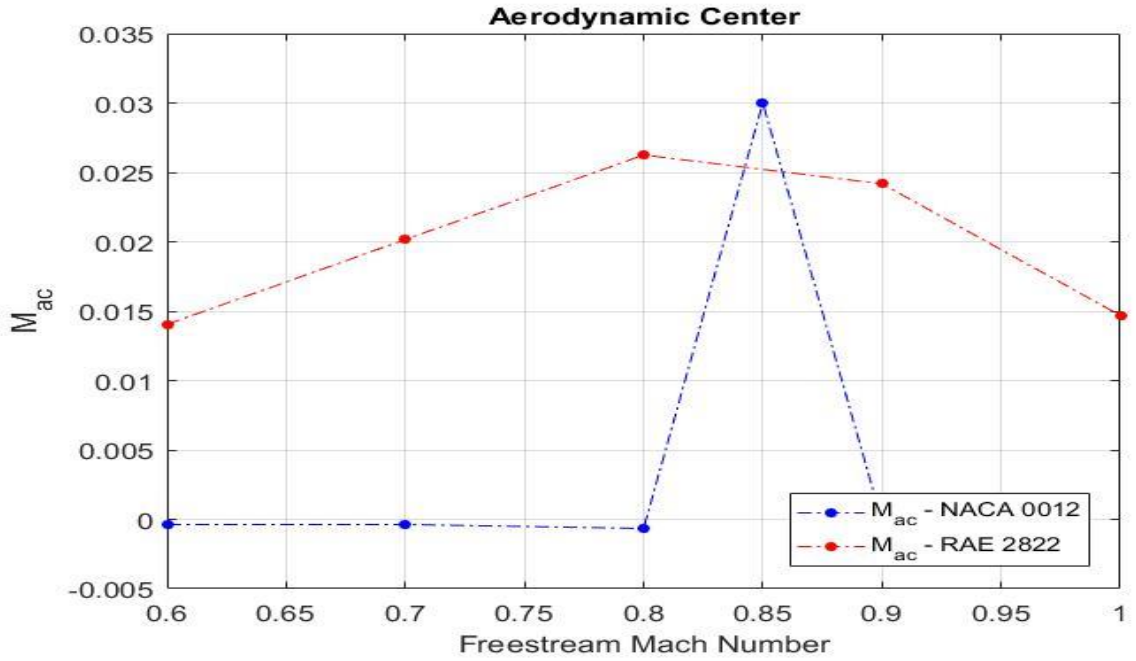

Figure 7.37 Variation of the moment about the aerodynamic M_{ac} center for the airfoils NACA 0012 and RAE 2822 with increasing free stream Mach number

Table 1 Numeric values of the x-coordinate and z-coordinate of the aerodynamic center and the moment about the aerodynamic center

NACA 0012			
Mach Number	Xac	Zac	Mac
0.600	0.268	-0.301	0.000
0.700	0.263	-0.608	0.000
0.800	0.305	1.536	-0.001
0.850	0.375	0.937	0.030
0.900	0.469	0.037	0.000
0.950	0.460	0.116	0.000

Table 2 Numeric values of the x-coordinate and z-coordinate of the aerodynamic center and the moment about the aerodynamic center

RAE 2822			
Mach Number	Xac	Zac	Mac
0.600	0.296	-0.457	0.014
0.700	0.315	-0.799	0.020
0.800	0.455	-0.117	0.026
0.900	0.457	-0.193	0.024
1.000	0.439	0.319	0.015

7.1.2. ADJOINT METHOD RESULTS

In this section, the results of the adjoint method simulations are presented. It is important to remember that the adjoint variables have no direct physical significance. Thus, it is difficult to analyze the results obtained from the simulations and make predictions if they are correct or not.

To be able to calculate the gradients of the position of the aerodynamic center and the moment about the aerodynamic center, the adjoint gradients of the pitching moment about the leading edge and the lift have to be obtained first. They can be directly calculated from the results of the adjoint simulation. The sensibilities of the lift are not presented in this work, but can be looked up in the study presented by Conç*a*lves Junior.

In Figure 7.38 and Figure 7.39 the variation of the sensibility of the pitching moment about the leading edge with respect to the stagnation temperature T_0 for the airfoils NACA 0012 and RAE 2822 with increasing Mach number, is displayed. The behavior for the two airfoils are very different. It is interesting to notice that the sensibility gradients of the pitching moment with respect to T_0 for NACA 0012 airfoil, resemble a lot the variation of the pitching moment presented in Figure 7.33, only that it is inverted.

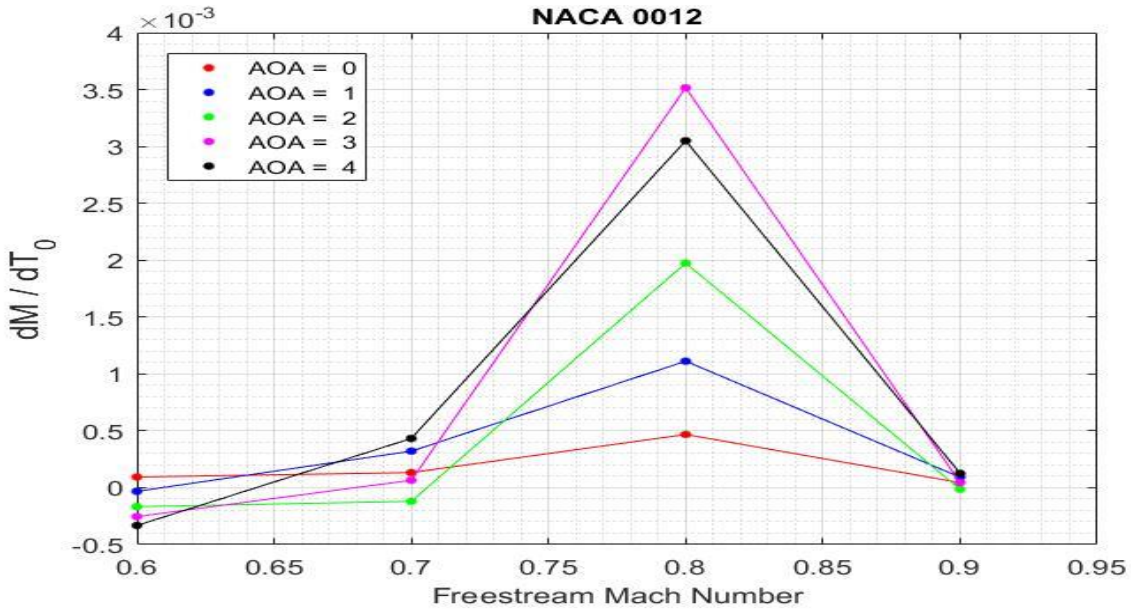

Figure 7.38 Variation of the sensibility of the pitching moment about the leading edge with respect to the stagnation temperature T_0 for the NACA 0012 airfoil with increasing Mach number

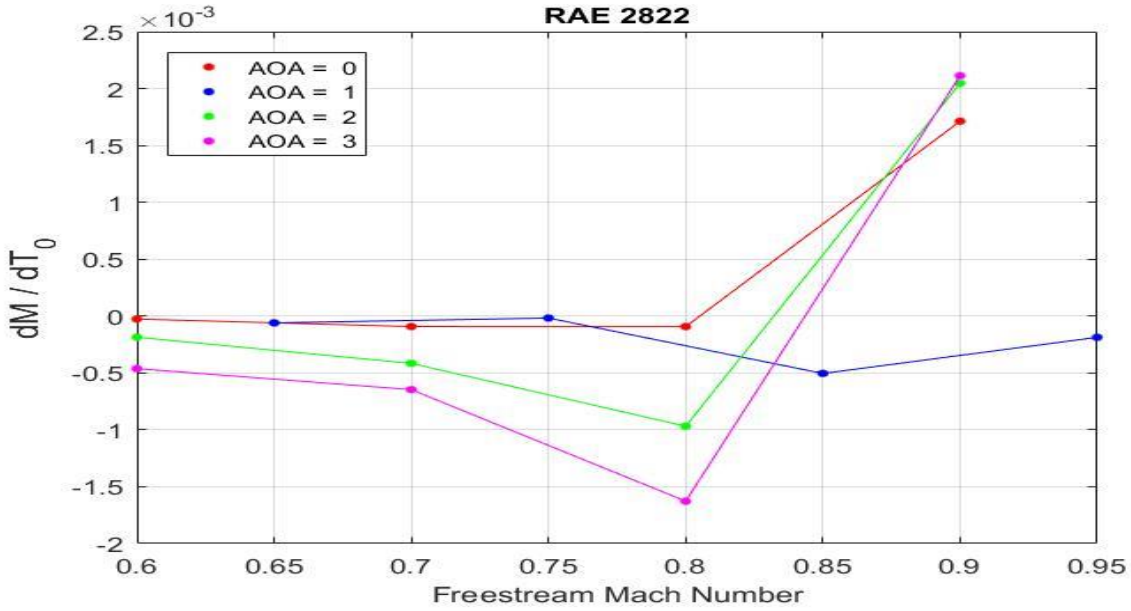

Figure 7.39 Variation of the sensibility of the pitching moment about the leading edge with respect to the stagnation temperature T_0 for the RAE 2822 airfoil with increasing Mach number

For α = 0.0°, the adjoint gradient stays around zero, with only a small deflection, whereas for the other angles of attack the adjoint gradient keeps increasing until Ma = 0.85, from where it starts decreasing again until a value close to zero for Ma =0.90. The adjoint gradient with respect to T_0 for the RAE 2822 airfoil shows the same behavior for all the presented angles of attack, except for α = 1.0°. For α = 1.0°, the gradient stays almost stable around a value of zero. For the other angles of attack the gradient decreases until Ma = 0.8, from where it increases steeply.

Next, the variation of the sensibility of the pitching moment about the leading edge with respect to the stagnation pressure p_0, with increasing Mach number is presented. Figure 7.40 shows the results for the NACA 0012 airfoil. The behavior is again similar for all the angles of attack, except for α = 0.0°. The plot resembles an inversion of the gradient presented above in Figure 7.38. The plot for the RAE 2822 airfoil shows the same behavior as the plot of the gradient with respect to T_0 but the values are significantly higher.

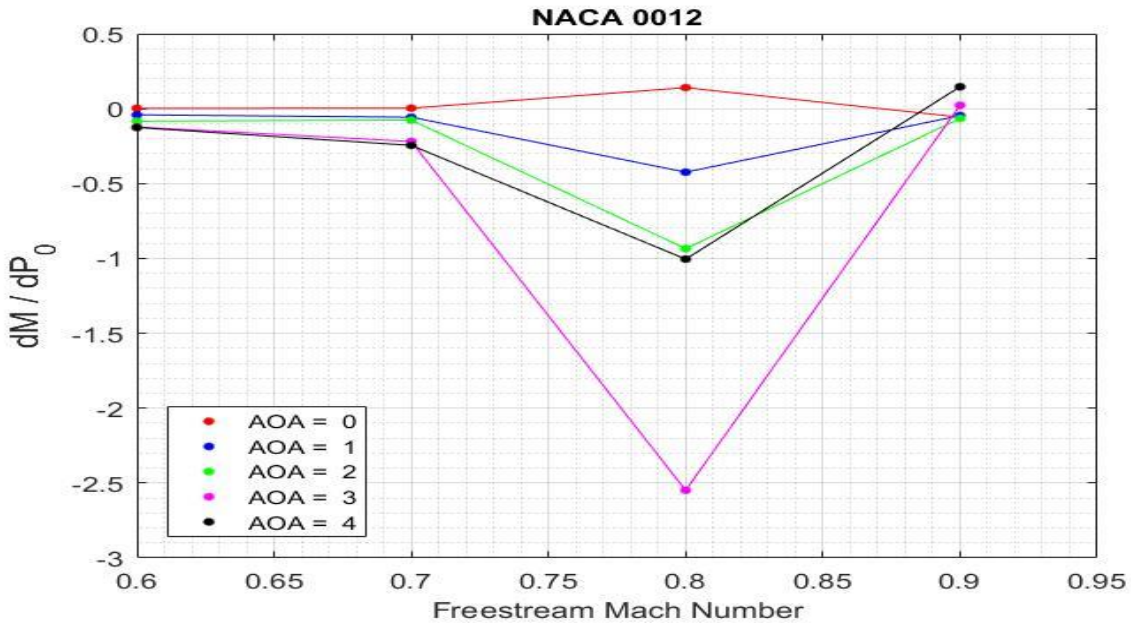

Figure 7.40 Variation of the sensibility of the pitching moment about the leading edge with respect to the stagnation pressure p_0 for the NACA 0012 airfoil with increasing Mach number

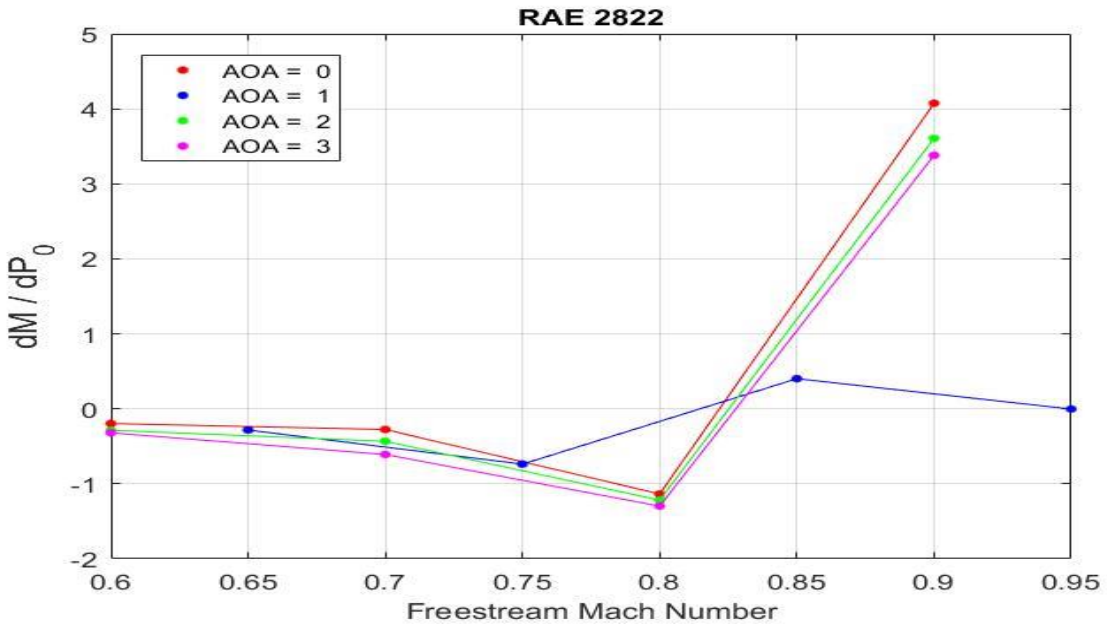

Figure 7.41 Variation of the sensibility of the pitching moment about the leading edge with respect to the stagnation pressure p_0 for the RAE 2822 airfoil with increasing Mach number

Finally, we get to the last objective of this study, the sensibility of the position of the aerodynamic center and the moment about the aerodynamic center with respect to the stagnation temperature T_0 and the stagnation pressure p_0.

In Table 3 and Table 4, the numeric values of the variation of the sensibilities of the position of the aerodynamic center and the moment about the aerodynamic center with respect to the stagnation temperature T_0 with increasing Mach number, are presented for the airfoils NACA 0012, and RAE 2822 respectively.

In Figure 7.42 the adjoint gradients of the x-coordinate ($\frac{\partial \mathrm{Xac}}{\partial T_0}$) with respect to T_0 are plotted for both airfoils. In the scope of this work it was not possible to obtain more results. The behavior for both airfoils is again completely different and their respective values have completely different magnitudes. For the NACA 0012 the obtained values are close to zero, with a great deviation at Ma = 0.80. For the RAE 2822, it can be observed, that the values are very small and alternating compared to the NACA 0012. At Ma = 0.60 the

results show a positive value, while for Ma = 0.70, the value is negative and for the last data point at Ma = 0.80 the value of the adjoint gradient is close to zero.

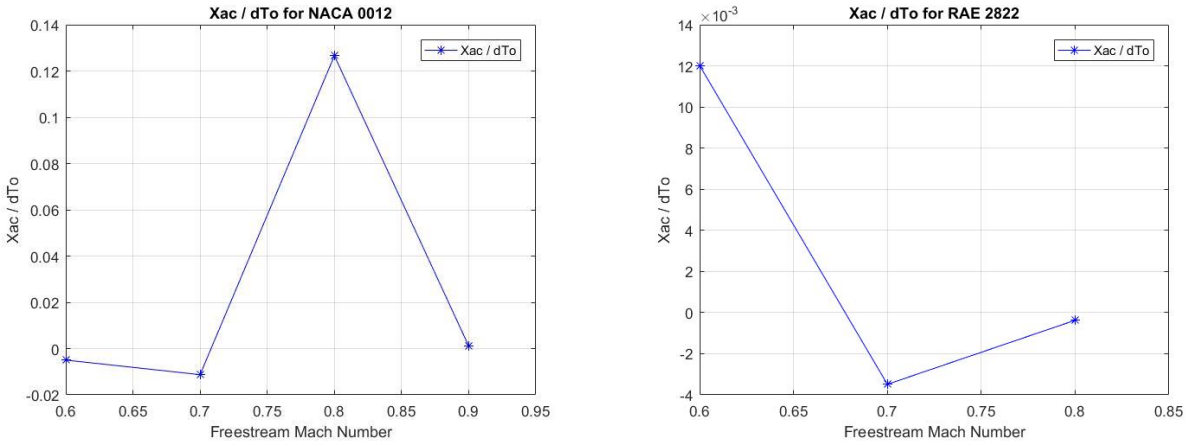

Figure 7.42 Variation of the sensibility of the x-coordinate of the aerodynamic center with respect to the stagnation temperature T_0 for the airfoils RAE 2822 and NACA 0012 with increasing Mach number

Figure 7.43 displays the adjoint gradients of the x-coordinate ($\frac{\partial \mathrm{Xac}}{\partial p_0}$) with respect to p_0 for both airfoils. The description of the plot for NACA 0012 is the same as above for the adjoint gradient with respect to T_0, only that the deflection at Ma = 0.80 is negative and with a value of $\frac{\partial \mathrm{Xac}}{\partial p_0}$ = 189.84, its magnitude is much greater. For the RAE 2822 airfoil we perceive a steep and almost linear increase from a negative value to a positive one.

The figures Figure 7.44 and Figure 7.45 represent the variation of the adjoint gradients of the z-coordinate of the aerodynamic center with respect to T_0, ($\frac{\partial \mathrm{Zac}}{\partial T_0}$), and p_0, ($\frac{\partial \mathrm{Zac}}{\partial p_0}$). The adjoint gradients with respect to T_0 for the NACA 0012 show a similar behavior to the behavior of $\frac{\partial \mathrm{Xac}}{\partial p_0}$. For the RAE 2822 the plot resembles the plot in Figure 7.42, only inverted. It increases from a negative value to a value close to zero, from where it decreases again.

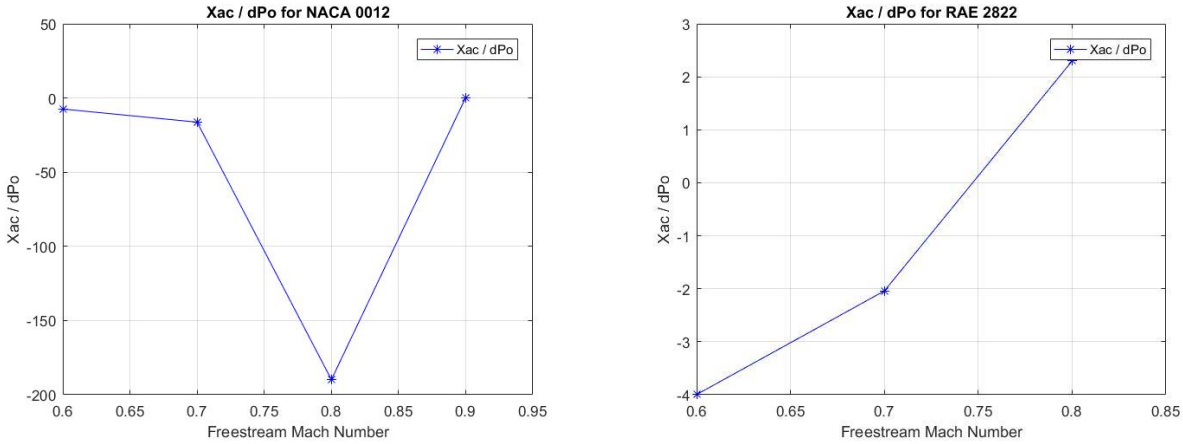

Figure 7.43 Variation of the sensibility of the x-coordinate of the aerodynamic center with respect to the stagnation pressure p_0 for the airfoils RAE 2822 and NACA 0012 with increasing Mach number

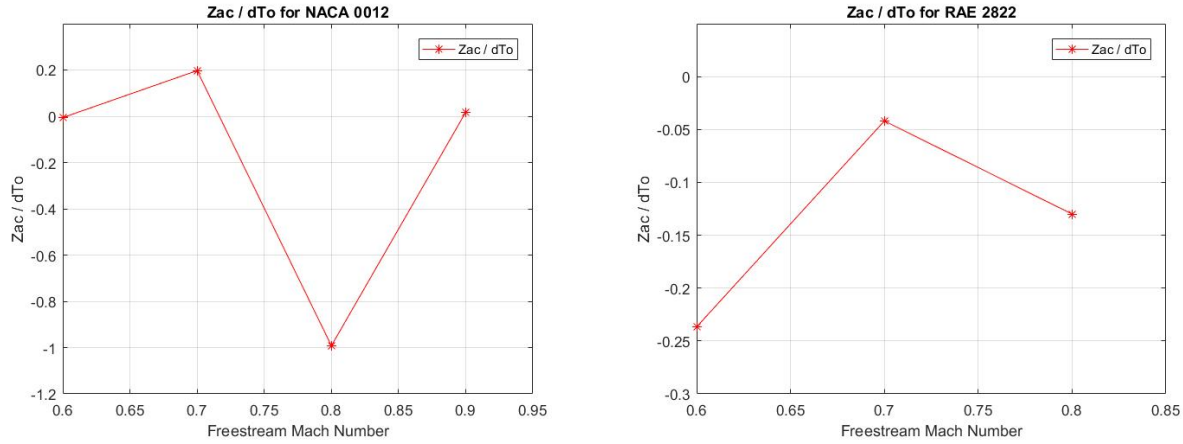

Figure 7.44 Variation of the sensibility of the z-coordinate of the aerodynamic center with respect to the stagnation temperature T_0 for the airfoils RAE 2822 and NACA 0012 with increasing Mach number

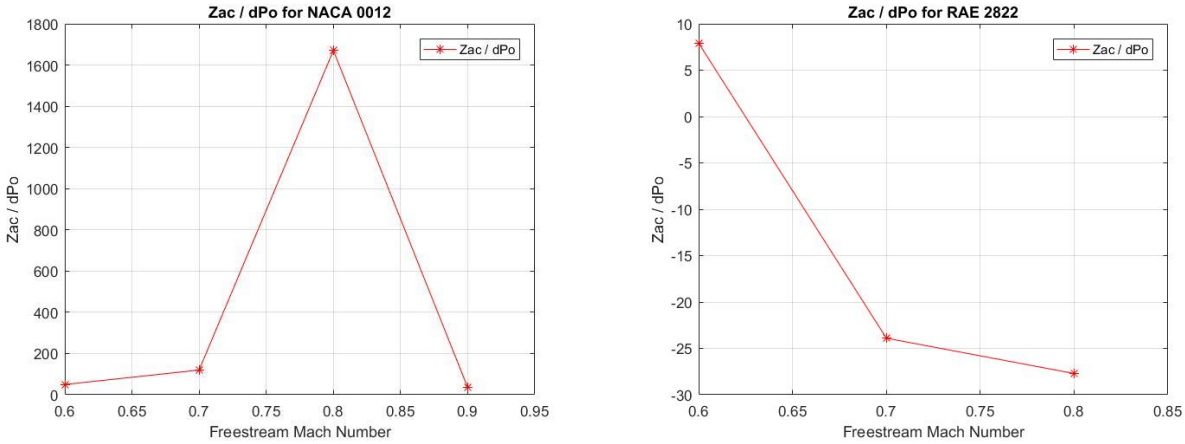

Figure 7.45 Variation of the sensibility of the z-coordinate of the aerodynamic center with respect to the stagnation pressure p_0 for the airfoils RAE 2822 and NACA 0012 with increasing Mach number

It is interesting to note, that the behavior of the adjoint gradients of the z-coordinate with respect to p_0, $(\frac{\partial \mathrm{Zac}}{\partial p_0})$, are almost identical with the adjoint gradients $\frac{\partial \mathrm{Xac}}{\partial T_0}$ for both airfoils represented in Figure 7.42. The only significant difference is that the values are of a very different magnitude, reaching for the NACA 0012 at Ma = 0.80, a value of 1670.4.

At last the variation of the sensibility of the moment about the aerodynamic center with respect to the stagnation temperature T_0, $(\frac{\partial \mathrm{Mac}}{\partial T_0})$, and the stagnation pressure p_0, $(\frac{\partial \mathrm{Mac}}{\partial p_0})$, is presented in the following two figures. For the NACA 0012 airfoil we can observer a contrary behavior for the adjoint gradients with respect to T_0, presented in Figure 7.46 and the adjoint gradients with respect to p_0, represented in Figure 7.47. $\frac{\partial \mathrm{Mac}}{\partial T_0}$ shows a negative deflection, whereas $\frac{\partial \mathrm{Mac}}{\partial p_0}$ shows a positive one. The plots for the RAE are not very similar. $\frac{\partial \mathrm{Mac}}{\partial T_0}$ increases from a negative value to a positive one, from where it drops again to a negative value. The $\frac{\partial \mathrm{Mac}}{\partial p_0}$ plot decreases continuously from a value close to zero to a

negative value. It should also be mentioned, that the magnitudes of the $\frac{\partial \mathrm{Mac}}{\partial p_0}$ values are a lot greater than the ones for $\frac{\partial \mathrm{Mac}}{\partial T_0}$.

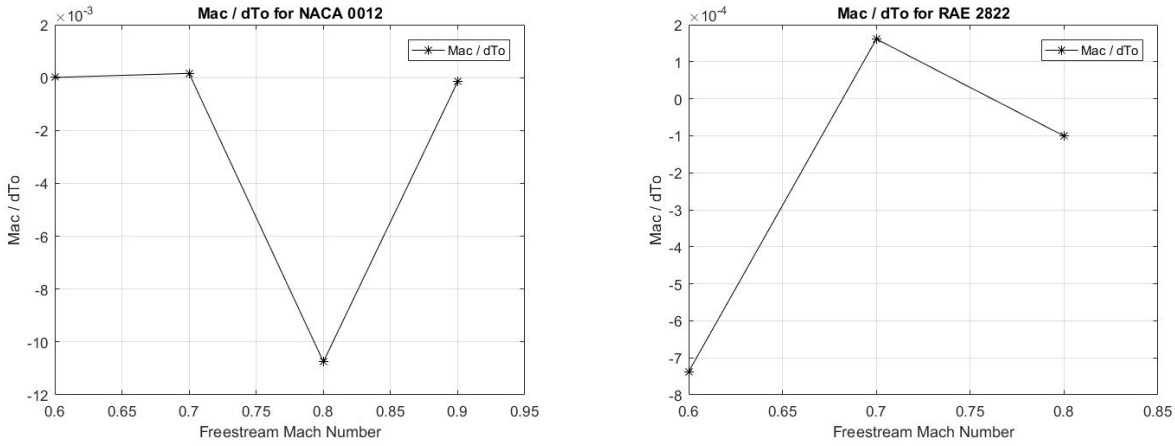

Figure 7.46 Variation of the sensibility of the moment about the aerodynamic center with respect to the stagnation temperature T_0 for the airfoils RAE 2822 and NACA 0012 with increasing Mach number

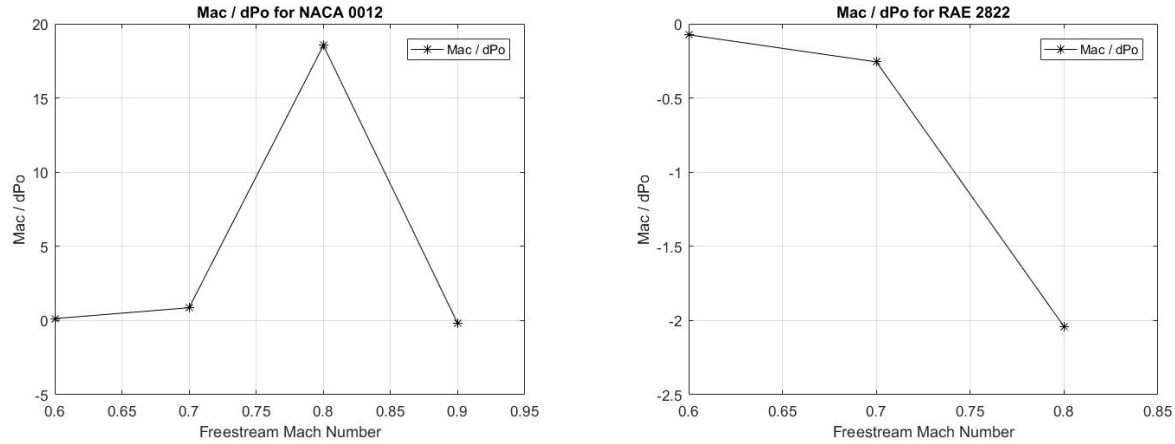

Figure 7.47 Variation of the sensibility of the moment about the aerodynamic center with respect to the stagnation pressure p_0 for the airfoils RAE 2822 and NACA 0012 with increasing Mach number

Table 3 Variation of the sensibilities of the x-coordinate and z-coordinate of the aerodynamic center and the moment about the aerodynamic center with respect to the stagnation temperature T_0 for the NACA 0012 airfoil with increasing Mach number

NACA 0012			
Mach Number	$\frac{\partial \mathrm{Xac}}{\partial T_0}$	$\frac{\partial \mathrm{Zac}}{\partial T_0}$	$\frac{\partial \mathrm{Mac}}{\partial T_0}$
0.600	-0.005	-0.006	0.000
0.700	-0.011	0.197	0.000
0.800	0.127	-0.992	-0.011
0.900	0.001	0.017	0.000

Table 4 Variation of the sensibilities of the x-coordinate and z-coordinate of the aerodynamic center and the moment about the aerodynamic center with respect to the stagnation temperature T_0 for the RAE 2822 airfoil with increasing Mach number

RAE 2822			
Mach Number	$\frac{\partial \mathrm{Xac}}{\partial T_0}$	$\frac{\partial \mathrm{Zac}}{\partial T_0}$	$\frac{\partial \mathrm{Mac}}{\partial T_0}$
0.6	0.01202	-0.23669	-0.00074
0.7	-0.00349	-0.04195	0.00016
0.8	-0.00037	-0.12999	-0.00010

Table 5 Variation of the sensibilities of the x-coordinate and z-coordinate of the aerodynamic center and the moment about the aerodynamic center with respect to the stagnation pressure p_0 for the NACA 0012 airfoil with increasing Mach number

NACA 0012			
Mach Number	$\frac{\partial \mathrm{Xac}}{\partial p_0}$	$\frac{\partial \mathrm{Zac}}{\partial p_0}$	$\frac{\partial \mathrm{Mac}}{\partial p_0}$
0.600	-7.458	49.677	0.133
0.700	-16.284	119.760	0.863
0.800	-189.840	1670.400	18.540
0.900	0.266	34.934	-0.199

Table 6 Variation of the sensibilities of the x-coordinate and z-coordinate of the aerodynamic center and the moment about the aerodynamic center with respect to the stagnation pressure p_0 for the RAE 2822 airfoil with increasing Mach number

RAE 2822			
Mach Number	$\frac{\partial \mathrm{Xac}}{\partial p_0}$	$\frac{\partial \mathrm{Zac}}{\partial p_0}$	$\frac{\partial \mathrm{Mac}}{\partial p_0}$
0.600	-3.996	7.914	-0.074
0.700	-2.041	-23.903	-0.257
0.800	2.299	-27.709	-2.041

8. CONCLUSIONS AND OUTLOOK

The objective of this work was to study the influence of compressibility on the aerodynamic center for 2-D airfoils at transonic speeds (Mach 0.6-0.95). Available Computational Fluid Dynamics codes, based on the Euler equations and the adjoint method were used to study these effects for the airfoils NACA 0012 and RAE 2822.

After a bibliographical review, the Euler flow simulations were conducted for Mach numbers in the transonic regime at various angles of attack. The results were post-processed in order to obtain the values for the following measures of merit: lift, drag, and pitching moment about the leading edge. These results were then used to calculate the position of the aerodynamic center and the moment about the aerodynamic center. Apart from that the results were used to calculate and plot the pressure coefficient values, in order to evaluate the solutions.

The obtained results were very satisfactory, as a consistency with the existing theories was proven. The simulations were able to capture the shift of the aerodynamic center form the 25% chord to 50% of the chord, as well as the appearance of shock waves and their shift towards the trailing edge with increasing Mach number for both airfoils. The link between the beginning of the aerodynamic center shift and the appearance of shock waves was established. The calculated measures of merit also showed a similar behavior as found in the literature. Only the results for the z-coordinate of the aerodynamic center for the NACA 0012 airfoil didn't provide the theoretically expected results and should therefore be subject to closer examination.

The Euler flow simulation results were then used as input for the simulations based on the adjoint method, in order to study the sensitivities of the aerodynamic center with respect to the stagnation pressure p_0 and the stagnation temperature T_0. Here, it is difficult to say if the obtained results were satisfactory or not as the adjoint variables have no direct physical significance, which complicates their validation. However, we

observe a greater sensitivity of the aerodynamic center with respect to stagnation temperature, than to the stagnation pressure.

Finally, for further research it would be very interesting to conduct more simulations, especially for the transonic regime to get a more detailed idea of the behavior of the measures of merit and the aerodynamic center. It would also be interesting to see, what results are obtained if the simulations are conducted for different airfoils and different types of meshes, to be able to compare and validate the results presented in this study.

9. BIBLIOGRAPHY

ADAMS, Nikolaus. **Fluidmechanik 1:** Einführung in die Dynamik der Fluide. Garching, 2010.

ANDERSON, John David. **Fundamentals of aerodynamics**. New York, NY: McGraw-Hill Education, 2017. 1130 p. (McGraw-Hill series in aeronautical and aerospace engineering). ISBN 9781259251344.

BARDOS, Claude; GOLSE, François; LEVERMORE, C. David. Fluid dynamic limits of kinetic equations II convergence proofs for the boltzmann equation. **Communications on Pure and Applied Mathematics**, v. 46, n. 5, p. 667–753, 1993. doi:10.1002/cpa.3160460503.

BÖSWIRTH, Leopold; BSCHORER, Sabine. **Technische Strömungslehre:** Lehr- und Übungsbuch. 10. ed. Wiesbaden: Springer Fachmedien Wiesbaden, 2014. Online-Ressource. ISBN 9783658056681.

CHRISTODOULOU, Demetrios. The Euler Equations of Compressible Fluid Flow. **Bulletin of the American Mathematical Society**, v. 44, n. 04, p. 581–603, 2007. doi:10.1090/S0273-0979-07-01181-0.

COLE, Julian D.; COOK, L. Pamela. **Transonic aerodynamics**. Amsterdam, New York: North-Holland, 1986. 473 p. (North-Holland series in applied mathematics and mechanics, v. 30). ISBN 9780444879585. Disponível em: <http://site.ebrary.com/lib/alltitles/docDetail.action?docID=10672517>.

ETKIN, Bernard. **Dynamics of Flight:** Stability and Control: Willey and Sons, 1996.

HAYASHI, Marcelo Tanaka. **Cálculo de sensibilidades não-geométricas em escoamentos modelados pelas equações de Euler compressíveis utilizando o método adjunto**. São Paulo, 2016.

HORNUNG, Mirko. **Flugzeugentwurf**. Garching, 2015.

JAMESON, Antony. Aerodynamic design via control theory. **Journal of Scientific Computing**, v. 3, n. 3, p. 233–260, 1988. doi:10.1007/BF01061285.

JUNGLAS, Peter. Kontinuitätsgleichung. Disponível em: <http://www.peter-junglas.de/fh/vorlesungen/stroemungslehre2/html/kap1-1-1.html>. Acesso em: 1 jun. 2017.

KARAMCHETI, Krishnamurthy. **Principles of ideal-fluid aerodynamics**. Malabar, Fla.: Krieger, 1980. 636 p. ISBN 0898741130.

KUETHE, Arnold Martin; CHOW, Chuen-yen. **Foundations of aerodynamics:** Bases of aerodynamic design. 5. ed. New York: Wiley, 1998. 572 p. ISBN 0471129194. Disponível em: <http://www.loc.gov/catdir/description/wiley032/97015257.html>.

LORENZ, J. **Die Navier-Stokes-Gleichungen für kompressible Flüssigkeiten**. Aachen, 1994.

SCHOLZ, Dieter; CIORNEI, Simona. Mach number, relative thickness, sweep and lift coefficient of the wing - An empirical investigation of parameters and equations. **Jahrbuch 2005**, 2005.